Nanoscale Horizons

Shape control with atomic precision: anisotropic nanoclusters of noble metals

Journal:	*Nanoscale Horizons*
Manuscript ID	NH-REV-04-2023-000125.R1
Article Type:	Review Article
Date Submitted by the Author:	12-Jun-2023
Complete List of Authors:	Li, Yingwei; Harvard University, Chemistry and Chemical Biology; Carnegie Mellon University, Chemistry Jin, Rongchao; Carnegie Mellon University, Chemistry

Nanoscale Horizons

REVIEW

Shape control with atomic precision: anisotropic nanoclusters of noble metals

Received 00th January 20xx,
Accepted 00th January 20xx

DOI: 10.1039/x0xx00000x

Yingwei Li,*[,†] and Rongchao Jin*

When plasmonic metal nanoparticles become smaller and smaller, a new class of nanomaterials — metal nanoclusters of atomic precision — comes to light and has become an attractive research topic in recent years. These ultrasmall nanoparticles (or nanoclusters) are unique in that they are molecularly uniform and pure, often possess a quantized electronic structure, and can grow into single crystals as do protein molecules. Exciting achievements have been made by correlating their properties with the precise structures at the atomic level, which has provided a profound understanding of some mysteries that could not be elucidated in the studies on conventional nanoparticles, such as the critical size at which plasmons are emergent. While most of the reported nanoclusters are spherical or quasi-spherical owing to the reduced surface energies (and hence stability), some anisotropic nanoclusters of high stability have also been obtained. Compared to the anisotropic plasmonic nanoparticles, the nanocluster counterparts such as rod-shaped nanoclusters can provide insights into the growth mechanisms of plasmonic nanoparticles at the early stage (i.e., nucleation), reveal the evolution of properties (e.g., optical), and offer new opportunities in catalysis, assembly, and other themes. In this Review, we highlight the anisotropic nanoclusters of atomic precision obtained so far, primarily gold, silver, and bimetallic ones. We focus on several aspects, including how such nanoclusters can be achieved by kinetic control, and how the anisotropy gives rise to new properties over the isotropic ones. The anisotropic nanoclusters are categorized into three types, i) dimeric, ii) rod-shaped, and iii) oblate-shaped nanoclusters. For future research, we expect that anisotropic nanoclusters will provide exciting opportunities for tailoring the physicochemical properties and thus lead to new developments in applications.

Introduction

One of the fundamental goals of nanoscience is to design and synthesize size- and shape-controllable materials at the nanometer scale.[1,2] It has been widely accepted that the physicochemical properties of metal nanoparticles (NPs) are highly dependent on their size and shape.[3–7]

Starting from Faraday's time and later developments by Turkevich, Frens, Schmid,[8–10] et al., the preparation of colloidal gold NPs of monodispersity has long been of major interest to researchers.[11] Ordered monolayers of alkanethiol-stabilized gold NPs with tunable interparticle spacing (by different lengths of alkane chains) were reported by Mulvaney and co-wokers.[12] Gold NPs functionalized by thiol-terminated DNA led to major research in nanobiomedicine.[13] A two-phase method was established by Brust et al, which stimulated interest in organic soluble Au NPs.[14] The Murray group demonstrated that the mean size of Au core can be adjusted by Au:thiolate ratio as well as temperature and the reduction rate.[15] In the meantime, Whetten et al. isolated a series of ultrasmall Au NPs with tight distributions and observed the molecular nature in the smaller cores of Au NPs.[16,17] In 2004, the Tsukuda group successfully separated different Au clusters (~1 nm, ranging from Au_{10} to Au_{39}) protected by glutathione via polyacrylamide gel electrophoresis, and their chemical compositions were precisely determined by electrospray ionization mass spectrometry (ESI-MS).[18,19] About three years later, crystallization was worked out and the total structures of $Au_{102}(SR)_{44}$ and $[Au_{25}(SR)_{18}]^-$ (SR = thiolate) nanoclusters (NCs) were solved by X-ray crystallography,[20–22] thus, a new age began, so-called atomically precise nanochemistry.[23–26] Since then, the research thrust on Au-SR NCs by the Jin group and others[24,27–30] has led to the creation of a series of noble metal NCs of atomic precision.

Department of Chemistry, Carnegie Mellon University, Pittsburgh, PA 15213, USA.
**E-mail: yingweil@alumni.cmu.edu (Y.L.); rongchao@andrew.cmu.edu (R.J.)*
[†]Present address: Department of Chemistry and Chemical Biology, Harvard University, Cambridge, MA 02138, USA.

Evolution from complexes to nanoclusters to nanoparticles

Scheme 1. The size evolution from Au(I)–L complexes, to Au(0/I)–L NCs, then to Au(0)–L NPs. (A) Binuclear Au(I)–L complex $Au_2(S_2PH_2)_2$ and its orbital diagram.[31] Redrawn by the authors. (B) The crystal structure of $Au_{25}(SR)_{18}^-$ NC and its molecular-like electronic structure of with HOMO–LUMO gaps (E_g) > 0. Reproduced with permission.[21] Copyright 2008, American Chemical Society. (C) The optical absorption spectra of isomeric $Au_{30}(SR)_{18}$-*hcp* and $Au_{30}(SR)_{18}$-*fcc* (the spectra are offset to avoid overlap). (D) The photographs of a series of adamantanethiol-protected NCs in CH_2Cl_2, from left to right: $Au_{16}(SR)_{12}$, $Au_{16}Ag_1(SR)_{13}$, $Au_{21}(SR)_{15}$, $Au_{22}(SR)_{16}$, $Au_{22}Cd_1(SR)_{16}$, $Au_{24}(SR)_{16}$, $Au_{29}(SR)_{19}$, $Au_{30}(SR)_{18}$-*fcc*, $Au_{30}(SR)_{18}$-*hcp*, and $Au_{36}Ag_2(SR)_{18}$. (C/D) Data collection performed by Y.L. (E) E_g of Au-SR NCs with I_h versus *fcc* and decahedral kernels as a function of the total number of Au atoms in NC. Reproduced with permission.[32] Copyright 2021 Wiley-VCH GmbH. (F) The size dependence of the electronic properties in atomically precise gold nanoparticles with a sharp transition from non-metallic $Au_{246}(SR)_{80}$ (E_g > 0) to metallic $Au_{279}(SR)_{84}$ (E_g = 0). Reproduced with permission.[33] Copyright 2021 The Author(s). (G) Optical extinction spectra of gold colloids (3–100-nm diameters), inset: photograph of 10-nm Au colloid, and the continuous band electronic structure of metallic-state NPs (E_f = Fermi level). Reproduced with permission.[24] Copyright 2016 American Chemical Society.

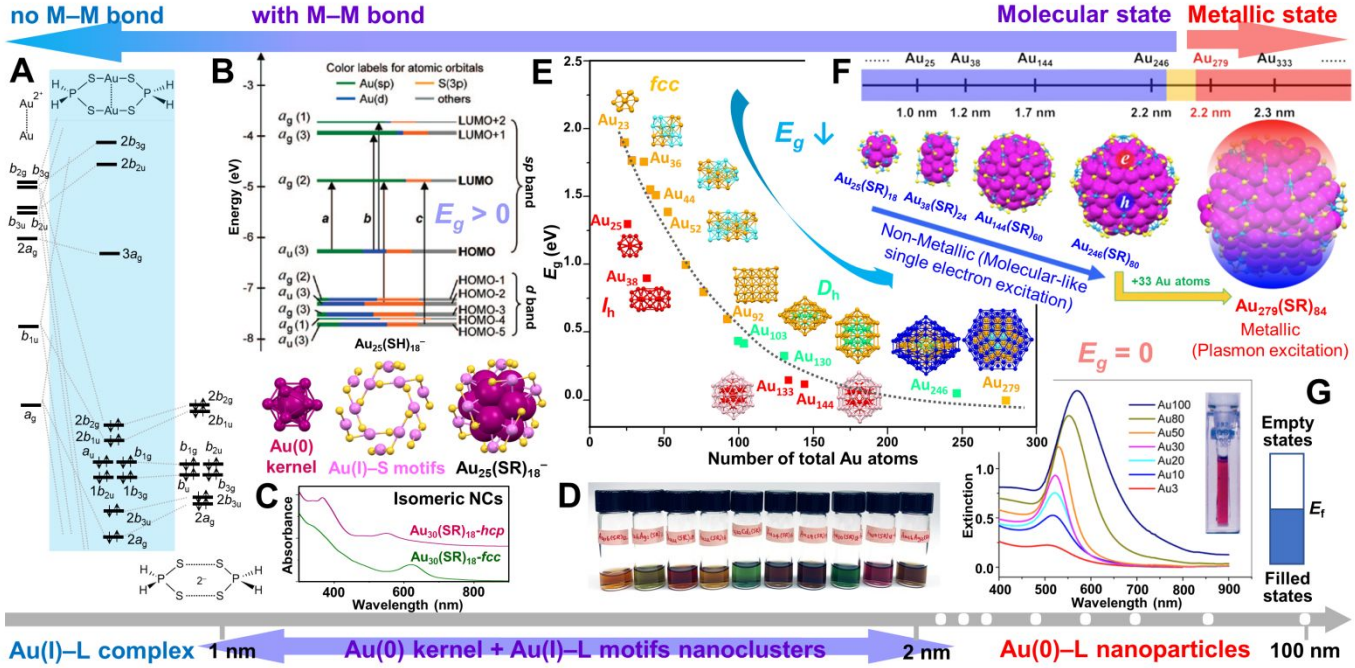

The metal (e.g., Au) NCs occupy a unique position in bridging up the metal–organic complexes and regular metal NPs, revealing the important molecule-to-metal transition (Scheme 1). A model binuclear Au(I)–L complex—$Au_2(S_2PH_2)_2$—and its orbital interaction diagram for Au_2^{2+} with two $S_2PH_2^-$ ligands (no *d* orbitals are included) are illustrated in Scheme 1A (simplified from the orignial work).[31] Substantial *s* and *p* mixing into the *d* block gives aurophilic interactions,[34] which is responsible for the tendency of Au(I) ions to clusters. Note that there is no metal–metal (M–M) bond in these Au(I)–L complexes. As the Au(I)–L precursor is reduced, Au–Au bonds form and give rise to a Au(0) kernel, which is the nucleation process at the initial stage of NP growth. To the surprise of nanochemists, at such an early stage, NCs with tens to hundreds of metal atoms (ultrasmall NPs) can also be very stable due to the passivation by ligands which are strongly bonded to the metal surface, as well as their close-shelled geometric structues (e.g., magic numbers) and/or electronic structures (e.g., superatoms).[35,36] Taking the most thoroughly studied $Au_{25}(SR)_{18}^-$ NC as example, it has an icosahedral (I_h) Au_{13} kernel and six $Au_2(SR)_3$ staple-like motifs at the interface (Scheme 1B, top), and the metal core (Au_{kernel} + Au_{motif}) is then wrapped inside an organic ligand shell. Almost all of the Au–thiolate NCs have such kernel-motif structures, but for NCs without any surface motif (e.g., Au–phosphine NCs), only a metal core is inside the ligand shell. Note that the oxidation state of the Au_{kernel} is not exactly 0, but between 0 and 1 with more Au(0) character. In addition, NCs have discrete energy levels with a distinct HOMO–LUMO gap (E_g > 0, HOMO = highest occupied molecular orbital, LUMO = lowest unoccupied molecular orbital) that are akin to molecules (Scheme 1B, bottom). A distinctive feature of NCs compared to complexes is that they have multiple free valence electrons to show unique optical properties with rich features (see Figure 1).[32] For example, isomeric $Au_{30}(SR)_{18}$ NCs (SR = adamantanethiolate) with both face-centered-cubic (*fcc*) and hexagonal-close-packed (*hcp*) kernels have been obtained by the Jin group,[37,38] and their absorption spectra are very different (Scheme 1C); note that the discussion on the *fcc* and *hcp* kernel structures is given in the section of "Rod-shaped nanoclusters". Remarkably, a series of Au-SR NCs protected by the same adamantanethiol ligands have been achieved, which exhibit an atom-by-atom addition evolution and various colors, including $Au_{16}(SR)_{12}$ (orange), $Au_{16}Ag_1(SR)_{13}$ (light green), $Au_{21}(SR)_{15}$ (red), $Au_{22}(SR)_{16}$ (light brown), $Au_{22}Cd_1(SR)_{16}$ (turquoise), $Au_{24}(SR)_{16}$ (greenish brown), $Au_{29}(SR)_{19}$ (brown), $Au_{30}(SR)_{18}$-*fcc* (green), $Au_{30}(SR)_{18}$-*hcp* (magenta), and $Au_{36}Ag_2(SR)_{18}$ (brown), although their sizes are very close (Scheme 1D). This phenomenon is

different from the chalcogen-bridged silver or copper clusters (Ag(I) or Cu(I/II) sulfides/selenides) by Fenske et al., which often show less features in absorption,[39,40] or the chalcogenide quantum dots with tunable band gaps by changing the composition,[33] or the metal NPs with surface plasmon resonance which, for example, shifts from 520 to 570 nm as the diameter of spherical Au NPs increases from ~10 to ~100 nm (Scheme 1G).[24]

The noble metal NCs show multiple absorption peaks and their energy gaps are very senstive to and highly tunable by size (i.e., the number of metal atoms), composition (e.g., doping or alloying) and structure (e.g., shape).[24-29] In general, the energy gap of atomically precise NCs decreases when the size of the NCs increase (Scheme 1E).[43] As the Au(0) kernel grows larger, however, the number of Au atoms in the Au(I)–S motifs does not change much: there are 12 Au_{motif} atoms in $Au_{25}(SR)_{18}$, and still 40 Au_{motif} in the much larger $Au_{246}(SR)_{80}$, indicating the Au(0)/Au(I) ratio increases when the NC becomes larger. Moreover, with atomically precise nanochemistry, a sharp transition from semiconducting $Au_{246}(SR)_{80}$ to metallic-state $Au_{279}(SR)_{84}$ with only 33 Au atoms in the growth (Scheme 1F) has been observed.[33,44] The $Au_{279}(SR)_{84}$ NC shows a quasicontinuous band electronic structure for metallic-state NPs. With the enlightenment by atomically precise NCs, we believe that the regular Au NPs should also have staple-like Au(I)–L surface structures although they cannot be fully resolved by transmission electron microscopy due to insufficient resolution and image contrast. But since the number of motif Au(I) atoms are quite small compared to the large Au(0) kernel, regular Au NPs are regarded as all Au(0) atoms of metallic state (E_g = 0, no energy gap between the conduction band and valence band), with tunable plasmon resonances as the size changes (Scheme 1G).

The advantages of achieving NCs at the atomically precise level are obvious: 1) although transmission electron microscopy (TEM) can determine the precise size and shape of NPs, analyze their chemical compositions, crystalline structures, and valence states, insufficient image contrast limits the identification of organic monolayer on the particle surface. By contrast, the inter- or intra-particle interactions between ligands — which are especially important in elucidating the self-assemblies in supercrystals — can be clearly determined for atomically precise NCs;[38,45–48] 2) for both quantification of adsorption and understanding of the catalytic mechanism, revealing the nature and structure of the active site(s) is critical since the interactions of active sites with substrates (i.e. reactants) can only be understood when the active site structure is known;[30,49–52] 3) the organic–inorganic interface of the nanostructure which is crucial for resolving the surface science can be fully unveiled with the total structure (metal core + ligand shell) solved, showing that the intrinsic origin of chirality of metal NCs is the chiral arrangements of interface atoms and motifs;[53–56] 4) not only a sharp transition from non-metallic $Au_{246}(SR)_{80}$ to metallic $Au_{279}(SR')_{84}$ is demonstrated,[44] the energy gaps of NCs are found to be related to different atomic packing modes (e.g. I_h vs. *fcc* or decahedral (D_h) kernels) due to the different distribution of electron wavefunctions in the Au-S entity (Scheme 1E).[32,43]

A brief introduction concerning the synthetic evolution from size controllable Au NPs to Au NCs is given. Note that there have been excellent reviews on noble metal NP syntheses,[57–62] thus in this Review, only selected works relating the size control of Au NPs are highlighted in order to introduce how atomically precise Au-SR NCs of different sizes are produced. For Au NPs larger than 5 nm, a digestive ripening process in excess thiol developed by Lin et al resulted in greatly narrowed size distribution and long-range-ordered superlattices.[63] Based on the seed-growth procedure—which has been a popular technique for decades,[64,65] Jana and Murphy prepared Au NPs in the range of 5-40 nm, of which the sizes can be manipulated by varying the ratio of seed to metal salt.[66] The size of single crystalline Au nanospheres could also be controlled by altering the size or volume of the seeds.[67] As shown in Figure 1A-D, the diameters of the Au nanospheres could be varied conveniently by changing the volume of the seed solution added to the reaction mixture. The precursor ratio to make size-controlled Au NPs[9] gives an opportunity to develop an advanced kinetic control for making atomically precise NCs.[24] In the typical Brust-Schiffrin method for Au-thiolate NPs, the Au:ligand:reductant molar ratio was 1:1.1:0.1.[14] By contrast, in the one-pot method to produce the atomically precise $Au_{25}(SR)_{18}$ NCs (SR = C_2H_4Ph), the molar ratio of Au:PhC_2H_4SH:reductant was 1:5:10.[68] The optical absorption spectrum, MALDI-mass spectrometry (MS) spectrum, and the corresponding single crystal structure of anionic $Au_{25}(SR)_{18}$ NC are shown in Figure 1E.[21]

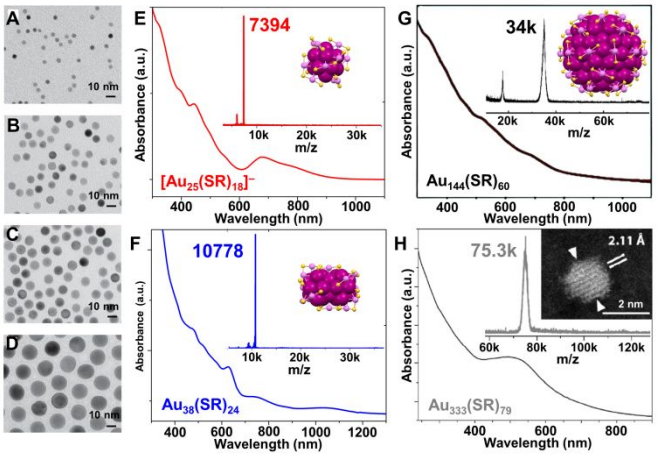

Figure 1. TEM images of single-crystalline Au nanospheres with controlled average diameters (A-D) 5, 8, 10, and 16 nm, by adding (A-D) 1000, 500, 50, and 20 μL Au seed solution, respectively. In Au seed solution preparation, the molar ratio of Au:ligand:reductant = 1:400:2.4. Reproduced with permission.[67] Copyright 2013, WILEY-VCH GmbH. UV-vis spectra, MALDI-MS spectra, and corresponding crystal structures or scanning-TEM image of (E) $[Au_{25}(SR)_{18}]^-$; (F) $Au_{38}(SR)_{24}$; (G) $Au_{144}(SR)_{60}$; and (H) $Au_{333}(SR)_{79}$ NCs. (E/F) Data collected by Y.L.; (G) Reproduced with permission.[69] Copyright 2022, The Authors, published by the Royal Society of Chemistry. (H) Reproduced with permission.[70,71] Copyright 2012/2019, The Authors, published by the National Academy of Sciences USA. Color codes: magenta/violet = Au, yellow = S, R groups are omitted for clarity.

As indicated by the above comparison, the successful synthesis of atomically precise Au-SR NCs usually go through two steps: 1) excess thiol is used to convert Au^{III} into Au^{I}–SR complexes (or polymers), and 2) a great excess of $NaBH_4$ is used to reduce Au^{I}-SR to Au(0). Moreover, the size control of

atomically precise NCs is no longer dependent on the seed size or its concentration since they are at the scale of seed size (i.e., ~1-3 nm in diameter).[72,73] Then, how can one obtain NCs of different sizes in a controllable manner just like what was achieved in the plasmonic NPs? The Jin group provided an early strategy—size-focusing—to create a chemical environment for the formation of an exclusive size of Au-SR NC while suppressing the formation of other sizes.[74] Specifically, the mass range of the initial product (i.e., $Au_x(SR)_y$ mixture) was first kinetically controlled by Au:thiol ratio, temperature, reducing rate, etc., and then the $Au_x(SR)_y$ mixture was etched at elevated temperatures and with excess thiol (i.e., thermodynamic selection for the most stable size), and finally $Au_{38}(SR)_{24}$ of molecular purity was achieved (Figure 1F).[75,76] The $Au_{144}(SR)_{60}$ NCs were obtained by etching for 24 h to eliminate impurities of small sizes (Figure 1G),[77] and the total structure of $Au_{144}(SR)_{60}$ was later solved by using $HSCH_2Ph$ instead of HSC_2H_4Ph in the initial synthesis (Figure 1G, inset).[78] When adjusting the Au:thiol molar ratio from 1:3 (for the preparation of $Au_{144}(SR)_{60}$) to 1:2, larger sized $Au_{333}(SR)_{79}$ was made (Figure 1H).[70,71] Other methodologies, including ligand-exchange-induced size and/or structure transformation,[79–84] ligand substituent group hindrance induced size selection,[85–88] heteroatom doping induced size/ structure transformation, metal exchange or anti-galvanic reduction,[89–92] have been developed to enrich the library of noble metal NCs during the past two decades.

The unique chemical and physical properties, especially the optical properties, of plasmonic NPs are not only determined by the number of metal atoms or size, but also by the shape of the core. Shape-controlled syntheses of NPs,[93–97] especially the anisotropic structures with gold nanorods as the most thoroughly studied one[98–102] were obtained in a convenient way around 2000. Different from the less tunable plasmon peak wavelength range of isotropic Au NPs of 4–200 nm, anisotropic Au nanorods permit one to drastically tune the longitudinal plasmon wavelength from the visible to near-infrared range by controlling the aspect ratio (AR) of rods. Over the past two decades, researchers have frequently taken the advantages of such specific phenomena to enable sensing applications,[103–105] plasmon-enhanced spectroscopies,[93,106–109] bio-imaging,[110,111] and photothermal therapy.[112–117]

The same trend has also been seen in the relatively short history of atomically precise metal-thiolate NCs, in which isotropic structures were obtained at the beginning of research since the spherical structures have less surface energy, that is, higher stability.[20,21,77,118] Fortunately, with the advances in synthetic methods, we have witnessed more and more cases on non-spherical NCs. Spheroidal shapes (Scheme 1) are found in large-sized NCs with more than 100 metal atoms. For example, $Au_{130}(SR)_{50}$ is the first reported NC to have multiple concentric shells with a barrel-shaped structure,[88] but only with a small aspect ratio (AR = 1.13). The $Ag@Au_{17}@Ag_{27}@Au_{17}(C{\equiv}CR)_{34}$ structure exhibits a spheroidal shape with AR = 1.26, and this $Au_{34}Ag_{28}(C{\equiv}CR)_{34}$ NC shows much better catalytic performance in its intact form than the partially or completely ligand-removed NCs.[119] AR of 1.17 is found in the $Au_{156}(C{\equiv}CR)_{60}$ NC, which is in the transition region from molecular to metallic state.[120] These spheroidal shapes are at the borderline between isotropic and anisotropic structures, and will not be the focus in this review. Larger AR values are highly desirable from the shape effect point of view.

Herein, we focus on the works on noble metal NCs of atomic precision with anisotropic structures in the past 15 years to highlight their distinctive chemical and physical properties. Some illustrations are collected in Scheme 2. We divide the anisotropic NCs into three categories—dimeric structures, rod shapes and oblate (or disk-shaped) structures. Homoleptic Au and Au-based NCs (ligands including thiol, phosphine, and alkynyl) will be our primary coverage, whereas multileptic NCs, and Ag- and Cu-based NCs will be selectively discussed as supplementary cases. Note that we eliminate the charges and counter ions on most of the NCs in the Review for the simplicity of the formulas, unless those specifics become necessary in the discussion of electronic properties of the anisotropic NCs.

Scheme 2. Selected anisotropic Au and Au-based NCs of atomic precision and their corresponding properties. Dimeric structures include: (A) $Au_{38}(SR)_{24}$ and the circular dichroism spectra of its two enantiomers. Reproduced with permission.[121] Copyright 2013 Wiley-VCH GmbH; (B) $Au_{18}Ag_3Cd_1(SR)_{15}Br$ and its assembly in supercrystals.[122] Redrawn by the authors; (C) kinetic traces of nanosecond transient absorption for $Au_{29}(SR)_{19}$ and $Au_{30}(SR)_{18}$, and spectra of absorbance, emission and excitation for $Au_{29}(SR)_{19}$. Reproduced with permission.[38] Copyright 2021 Springer Nature Limited; (D) $Au_{22}(dppo)_6$ and the CO oxidation of $Au_{22}(dppo)_6/TiO_2$ catalyst pretreated in O_2 at different temperatures. Reproduced with permission.[123] Copyright 2016 American Chemical Society; (E) $Au_{24}H_3(NHC)_{14}Cl_2$ and its electrochemical CO_2 reduction performance at different current densities. Reproduced with permission.[124] Copyright 2022 American Chemical Society; Rod-shaped structures include: (F) the *fcc* series and absorption spectra. Reproduced with permission.[125] Copyright 2020 Wiley-VCH GmbH; (G) $Au_{24}(SR)_{20}$ and $Au_{24}(SeR)_{20}$ and the photographs of their solutions or solids under visible and UV light irradiation. Reproduced with permission.[126] Copyright 2016 Wiley-VCH GmbH; (H) $Au_{42}(SR)_{32}$ and its temperature changes upon irradiation compared to $Au_{38}(SR)_{24}$, $Au_{52}(SR)_{32}$, $Au_{24}(SR)_{20}$, and time-dependent images of $Au_{42}(SR)_{32}$ solution upon irradiation; temperature-dependent PL spectra of $Au_{42}(SR)_{32}$ solution. Reproduced with permission.[127,128] Copyright 2022 American Chemical Society; (I) $Au_6(dppp)_4$, $Au_8(dppp)_4Cl_2$, $Au_{11}(dppe)_6$ and their absorption spectra. Reproduced with permission.[129] Copyright 2013 American Chemical Society; (J) $Au_{37}(SR)_{10}(PPh_3)_{10}Cl_2$, $Au_{25}(SR)_5(PPh_3)_{10}Cl_2$, $Au_{24}(SR)_5(PPh_3)_{10}Cl_2$, $Au_{13}(dppe)_5Cl_2$, and their absorption spectra. Reproduced with permission.[130] Copyright 2017 National Academy of Science. Oblate-shaped structures include: (K) $Au_{22}(C{\equiv}CR)_{18}$ and its UV−vis spectra, PL spectra and lifetimes with different ligands. Reproduced with permission.[131] Copyright 2019 American Chemical Society; (L) $Au_{36}Ag_2(SR)_{18}$ and its HER electocatalytic activity compared to $Au_{38}(SR)_{24}$ and $Au_{25}(SR)_{18}^-$. Reproduced with permission.[132] Copyright 2021 American Chemical Society; (M) $Au_{56}(SR)_{24}(PR_3)_6Br_2$ and the kinetic traces of its transient absorption, and corresponding fits at selected wavelengths, and spectra at selected time-delays. Reproduced with permission.[133] Copyright 2022 The Author(s). Spheroidal structures include: $Au_{130}(SR)_{50}$ and $Au_{156}(C{\equiv}CR)_{60}$. The structures are redrawn from the cif in ref.[88,120]

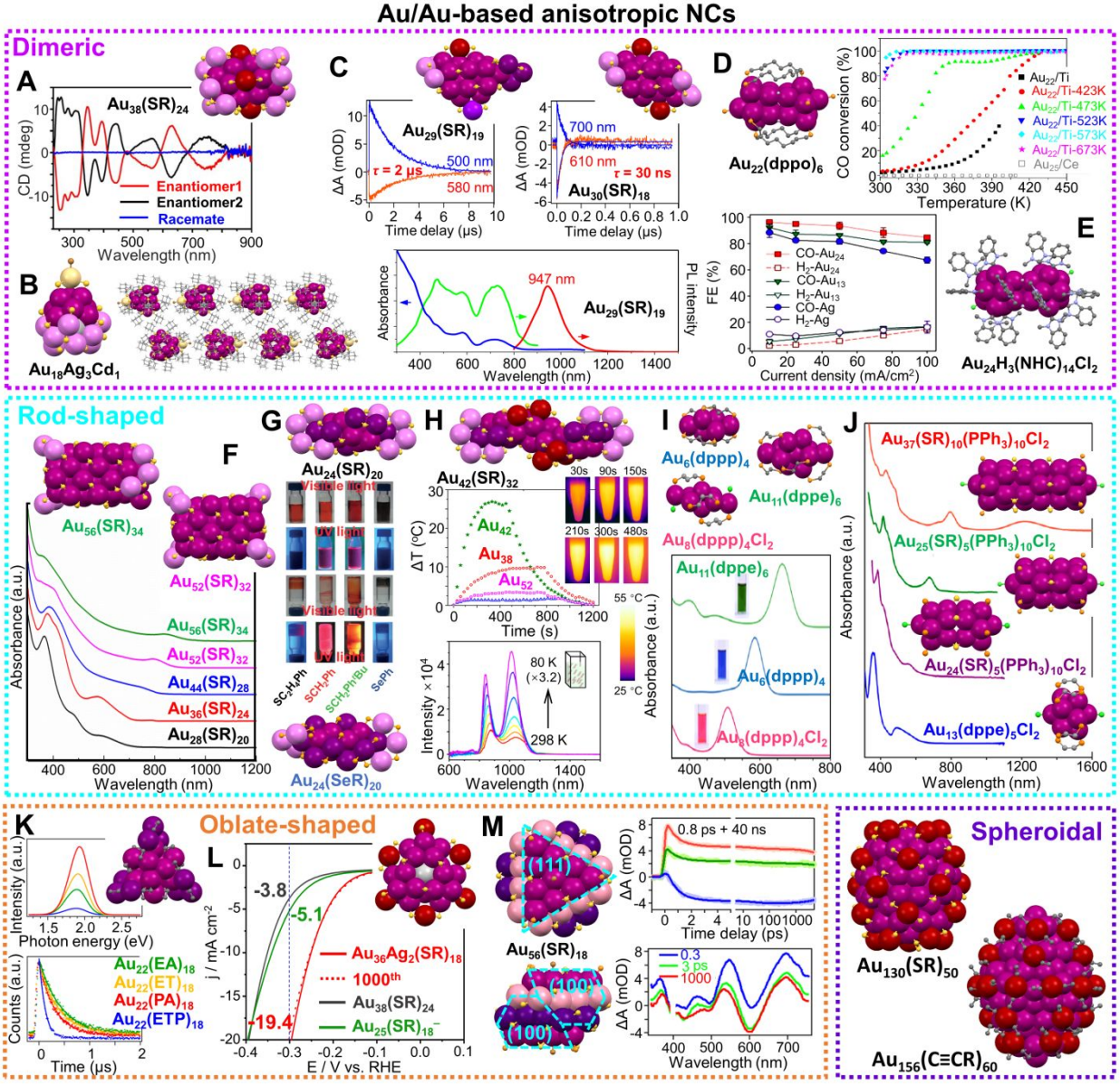

Dimeric nanoclusters

Plasmonic Au NP dimers and trimers can be constructed and separated in high purity,[134] and such nanostructures have been used for surface-enhanced Raman spectroscopy.[135] In terms of structural control, those dimers and trimers are formed by NPs attracting each other without any bond (i.e., with a subnanometer or larger gap between NPs). By contrast, when dimerization or trimerization occurs in atomically precise NCs, monomeric units are linked by metal–metal bonds inside a single particle. Thus, NC dimers can be regarded as the simplest anisotropic structures.

Y. Zhu et al. found that two $Au_{25}(SR)_{18}$ (SR = SC_2H_4Ph) monomers could be linked by two Ag atoms to form a $Au_{50}Ag_2(SR)_{36}$ dimer (Figure 2A, left).[136] Although the optical absorption spectrum does not show distinct differences when two monomers are bridged (Figure 2A, right), normalized partial density of states diagrams indicate that Ag^I has an influence on the HOMO of the dimer, causing band broadening. Moreover, the $Au_{50}Ag_2(SR)_{36}/CeO_2$ catalyst exhibited enhanced activity for CO oxidation compared to $Au_{25}(SR)_{18}/CeO_2$, while the catalyst based on $Au_{25-x}Ag_x(SR)_{18}$ NCs was of much less activity (Figure 2B).[136]

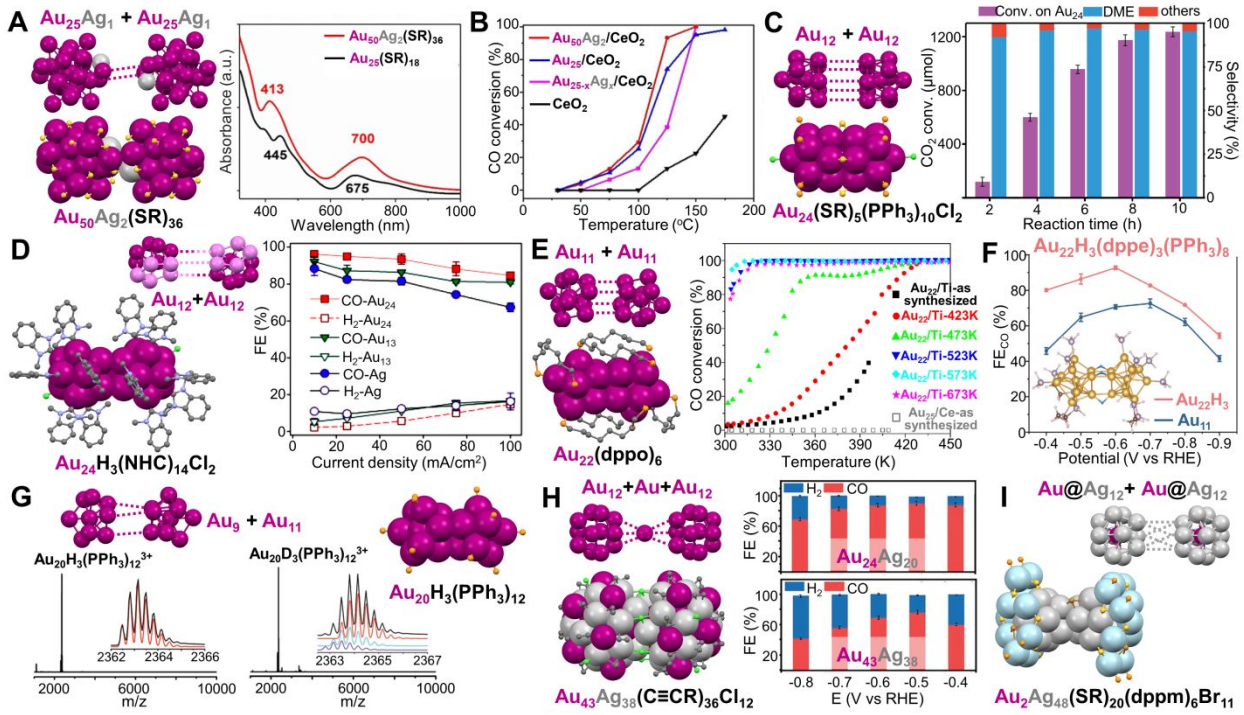

Figure 2. (A) Dimeric $Au_{50}Ag_2(SR)_{36}$ and its UV-vis spectrum compared to monomeric $Au_{25}(SR)_{18}$. (B) CO oxidation profiles of $Au_{50}Ag_2(SR)_{36}$, $Au_{25}(SR)_{18}$, and $Au_{25-x}Ag_x(SR)_{18}$ catalysts supported on CeO_2. Reproduced with permission.[136] Copyright 2020, Wiley-VCH GmbH. (C) $Au_{24}(SR)_5(PPh_3)_{10}Cl_2$ and the CO_2 hydrogenation on Au_{24}/SiO_2 catalysts with respect to reaction time. Reaction conditions: Au_{24}/SiO_2 (0.5% Au) 100 mg, 2 MPa reaction gas (CO_2:H_2 = 1:3) with 5% N_2, H_2O 15 mL, 130 °C. Reproduced with permission.[137] Copyright 2020, American Chemical Society. (D) $Au_{24}H_3(NHC)_{14}Cl_2$ and its electrochemical CO_2 reduction performance compared to $Au_{13}(NHC)_9Cl_3$ NCs and Ag NPs at different current densities. Reproduced with permission.[124] Copyright 2022, American Chemical Society. (E) $Au_{22}(dppo)_6$ and the CO oxidation curves of the $Au_{22}(dppo)_6/TiO_2$ catalysts pretreated in O_2 at different temperatures. Reproduced with permission.[123] Copyright 2016, American Chemical Society. (F) Electrocatalytic reduction of CO_2 to CO based on $Au_{22}H_3(dppe)_3(PPh_3)_8$ catalyst compared to $Au_{11}(dppe)_5$, inset: the theoretical structure of $Au_{22}H_3(dppe)_3(PPh_3)_8$. Reproduced with permission.[138] Copyright 2022, American Chemical Society. (G) The structure and mass spectra of $Au_{20}H_3(PPh_3)_{12}$ and $Au_{20}D_3(PPh_3)_{12}$. Reproduced with permission.[139] Copyright 2020, The Royal Society of Chemistry. (H) $Au_{43}Ag_{38}(C{\equiv}CR)_{36}Cl_{12}$ and its CO_2 reduction performance compared to $Au_{24}Ag_{20}(C{\equiv}CR)_{24}Cl_2$. Reproduced with permission.[140] Copyright 2022, The Author(s). (I) $Au_2Ag_{48}(SR)_{20}(dppm)_6Br_{11}$. Color codes: magenta/violet = Au, light grey/light blue = Ag, light orange = P, yellow = S, green = Cl, brown = Br, light purple = N, and grey = C, R groups are omitted for clarity.

Multi-ligand-protected NCs composed of two connected monomeric units without staple motifs have been studied as well, and these NCs also show interesting catalytic properties. In the process of making rod-shaped $Au_{25}(SR)_5(PPh_3)_{10}Cl_2$ (SR = SC_2H_4Ph), adding excess PPh_3 resulted in $Au_{24}(SR)_5(PPh_3)_{10}Cl_2$ consisting of two Au_{12} units (one vertex missing) joined together in an eclipsed manner (Figure 2C, left).[141] Further work indicated that the internal vacancy (i.e., the missing vertex) could provide $Au_{24}(SR)_5(PPh_3)_{10}Cl_2$ with more structural flexibility and mitigate the deactivation of the Au_{24}/SiO_2 catalysts which efficiently converted CO_2 to dimethyl ether (DME) (Figure 2C, right).[137] When the open pentagonal faces of the two incomplete I_h Au_{12} units rotated by ~120° with respect to each other, an N-heterocyclic carbenes (NHC) stabilized

NC—$Au_{24}H_3(NHC)_{14}Cl_2$—was obtained by the Crudden group (Figure 2D, left).[124] Three bridging hydrides were not resolved by X-ray analysis but were predicted to be located at the connection points by density-functional theory (DFT). Using a membrane electrode assembly electrochemical cell in which the cathode and anode were pressed against an anion exchange membrane, $Au_{24}H_3(NHC)_{14}Cl_2$ was tested for CO_2 electroreduction to CO, and the dimeric NC-based catalyst exhibited higher selectivity (i.e., Faradaic efficiency) than the catalysts of monomeric $Au_{13}(NHC)_9Cl_3$ and benchmark Ag NPs at all tested current densities (Figure 2D, right).[124]

L.-S. Wang et al. reported a $Au_{22}(dppo)_6$ (dppo = $Ph_2P(CH_2)_8PPh_2$) NC with two Au_{11} units clipped together by four dppo ligands (Figure 2E, left).[142] Low-temperature CO oxidation activity was observed for the $Au_{22}(dppo)_6/TiO_2$ catalyst pretreated in O_2 at different temperatures without ligand removal (Figure 2E, right).[123] Recently, the group found that $Au_{22}(dppo)_6$ gradually transformed *via* H evolution from $Au_{22}H_4(dppo)_6$ of which the tetrahydrides were confirmed by electrospray ionization MS and DFT calculations.[143] In another work, three hydrides were determined on heteroleptic $Au_{22}H_3(dppe)_3(PPh_3)_8$ (dppe = $Ph_2P(CH_2)_2PPh_2$ by ESI-MS and ^{1}H-NMR, and the structure was proposed to have two Au_{11} units connected at six Au sites and bridged by three H (Figure 2F, inset). The six bridged Au atoms in the trihydrido-NC were found to be critical in catalyzing electrochemical CO_2 reduction to CO, and a 92.7% Faradaic efficiency at –0.6 V vs RHE and high activity (134 A/g_{Au} mass activity) were obtained (Figure 2F).[138] Beside the homodimeric Au NCs, the Q.-M. Wang group demonstrated an $Au_{20}H_3(PPh_3)_{12}$ NC with a heterodimeric core, i.e., an Au_9 unit was connected to an Au_{11} unit (Figure 2G). The presence of trihydrides on Au was probed by ESI-MS and ^{1}H-NMR, and the hydrido-Au NC showed good stability for long-time storage.[139]

When two hollow I_h Au_{12} units are linked by one additional Au atom to form a dimeric kernel which is enclosed by a bimetallic shell, an $Au_{43}Ag_{38}(C{\equiv}CR)_{36}Cl_{12}$ NC is obtained (Figure 2H, left). Compared to $Au_{24}Ag_{20}(C{\equiv}CR)_{36}Cl_4$ with a monomeric kernel and a superatomic electronic configuration, the $Au_{43}Ag_{38}(C{\equiv}CR)_{36}Cl_{12}$ NC shows less activity in catalytic reduction of CO_2 to CO (Figure 2H, right).[140] This is in contrast to the observations in the hyrido-Au cases, i.e., dimeric $Au_{22}H_3(dppe)_3(PPh_3)_8$ and $Au_{24}H_3(NHC)_{14}Cl_2$ are better than their monomeric counterparts (Figure 2D/2F). We suppose that the hydrides and chlorides at the bridging sites are responsible for the catalytic difference. Besides, two Au@Au_{12} superatomic units ($1S^21P^6$) can also be combined into a dimeric kernel which is protected by different surface Ag motifs to form $[Au_2Ag_{42}(SR)_{27}]^+$ and $[Au_2Ag_{48}(SR)_{20}(dppm)_6Br_{11}]^{3+}$, respectively (dppm = $Ph_2PCH_2PPh_2$, Figure 2I).[144] DFT indicates the valence electronic structures of both NCs are analogous to that of Ne_2.

Another category of dimeric NCs have kernels formed by fusion of two I_h monomeric units. Jin et al. first solved the total structure of $Au_{38}(SR)_{24}$ (SR = SC_2H_4Ph) with a dimeric kernel as another benchmark NC[76] (in addition to the $Au_{25}(SR)_{18}$ in earlier work). Since then, $Au_{38}(SR)_{24}$ remains actively studied to establish extensive structure-property correlations in atomically precise nanomaterials. The dimeric Au_{23} kernel is composed of two I_h Au_{13} units fused together via sharing a common Au_3 face, i.e., Au_{13} + Au_{13} – Au_3. The Au_{23} kernel is further protected by six $Au_2(SR)_3$ and three $Au_3(SR)_4$ staples in a chiral configuration (Figure 3A),[76] consistent with the DFT calculations by Aikens et. al.[145] Compared to the superatom model of $(1S)^2(1P)^6(1D)^6$ for a $14e^-$ NC, a theoretical study based on supervalence bond (SVB) model does a better job in demonstrating that the electronic configuration of the Au_{23} kernel is $(1\Sigma)^2(1\Sigma^*)^2(1\Pi)^4(2\Sigma)^2(1\Pi^*)^4$, where each orbital is created by the bonding and antibonding interactions between the 1S and 1P superatomic orbitals of the two I_h Au_{13} units.[146,147] In this way, the SVB model relates the $Au_{23}(14e^-)$ kernel to an isoelectronic analog of the F_2 molecule (Figure 3B). Based on the structure of $Au_{38}(SR)_{24}$, a systematic ligand-exchange study revealed that *ortho*-substituted benzenethiols could preserve the $Au_{38}(SR)_{24}$ structure, while *para*- or non-substituted benzenethiols would cause the transformation of $Au_{38}(SR)_{24}$ into $Au_{36}(SR'')_{24}$.[148] In $Au_{38}(SC_2H_4Ph)_{24}$, the six $Au_2(SR)_3$ motifs resemble two tri-blade fans at the top and bottom, being arranged in a staggered conformation by ~60° to each other (Figure 3C, left);[76] by contrast, when applying an *ortho*-substituted aromatic thiol, the crystal structure of $Au_{38}(SR')_{24}$ (SR' = SPh–2,4$(CH_3)_2$) shows that one fan rotates only by ~45° relative to the other along the C_3 axis (Figure 3C, right). As a result, each $Au(SR')_2$ motif is parallel to the two adjacent $Au_2(SR')_3$ motifs at the waist of the $Au_{38}(SR')_{24}$ structure (Figure 3C, indicated by blue lines).[148] The dimeric $Au_{38}(SR)_{24}$ NC shows a series of absorption peaks, with the first band (i.e., the lowest energy) centered at 1050 nm (see Figure 1F),[75] which is significantly red-shifted from that of $Au_{25}(SR)_{18}$ with a mono-I_h Au_{13} kernel (its first absorption band at 780 nm).[149]

In light of the successful synthesis and crystallization of $Au_{38}(SR)_{24}$, heteroatom doping was investigated subsequently. Co-reducing Au^I-SR and Ag^I-SR, followed by thermo-etching with excess thiol, $Au_{38-x}Ag_x(SR)_{24}$ was resulted (x = 1–6, SR = SC_2H_4Ph) with the 1050 and 750 nm absorption bands blue-shifted and diminished at higher Ag dopants.[150] Crystallography shows that the doped Ag atoms are distributed in the kernel on the middle fusion plane and the two ends.[151] By contrast, $Au_{38-x}Cu_x(SR')_{24}$ (x = 0–6, SR' = SPh–2,4$(CH_3)_2$) obtained by a ligand exchange method demonstrates that all Cu atoms are selectively doped in the trimeric motifs, and the optical absorption spectrum remains the same as that of the homogold counterpart. This is reasonable since Cu dopants contribute little to the frontier orbitals.[152]

Doping the group 10 elements (i.e., Pd, Pt) into $Au_{38}(SR)_{24}$ provides a more interesting story. In 2011, Negishi et al. used size exclusion chromatography to separate $Pd_xAu_{38-x}(SR)_{24}$ (x = 1, 2), which was then heated at 60 °C for 8 days to preferentially decompose the singly doped NC. The resulted pure $Pd_2Au_{36}(SR)_{24}$ NC was found to be more stable than $Au_{38}(SR)_{24}$ against degradation.[153] Lee et al. used a similar method to produce $Au_{38}(SR'')_{24}$, $[Pd_2Au_{36}(SR'')_{24}]^0$ and $[Pt_2Au_{36}(SR'')_{24}]^{2-}$ (SR'' = SC_6H_{13}), and studied their optical and electronic properties.[154] X-ray photoelectron spectroscopy (XPS) shows the Pd^0 and Pt^0 state, indicating that both dopants are located

at the central positions of the bi-I_h kernel, in contrast to the observation of Pd–S bonds in the K-edge extended X-ray absorption fine-structure data.[155] Moreover, the Pt-doped NC is dianionic as two associated cations are observed by NMR analysis.[154] Voltametric investigations show that the HOMO–LUMO (highest occupied molecular orbital to lowest unoccupied molecular orbital) gap of $[Pt_2Au_{36}(SR'')_{24}]^{2-}$ ($14e^-$) is 0.95 eV, slightly larger than the 0.86 eV gap of $Au_{38}(SR'')_{24}$ ($14e^-$); whereas $[Pd_2Au_{36}(SR'')_{24}]^0$ shows a drastically decreased gap (0.26 eV) due to the Jahn-Teller distortion of the $12e^-$ NC (Figure 3D).

As mentioned above, the chiral arrangement of $Au_3(SR)_4$ motifs on the surface of Au_{23} kernel gives rise to the chirality of $Au_{38}(SR)_{24}$. Bürgi et al. first separated the two enantiomers by chiral high-performance liquid chromatography, showing mirror-image circular dichroism (CD) responses (Figure 3E) of $Au_{38}(SR)_{24}$ with large anisotropy factors (up to 4×10^{-3}).[121] The enantiomers with two doped Pd atoms show significantly changed CD spectra compared to their parent NCs (Figure 3F), although the anisotropy factors are of similar magnitude. However, the doped 38-metal NCs undergo racemization at a much lower temperature.[156]

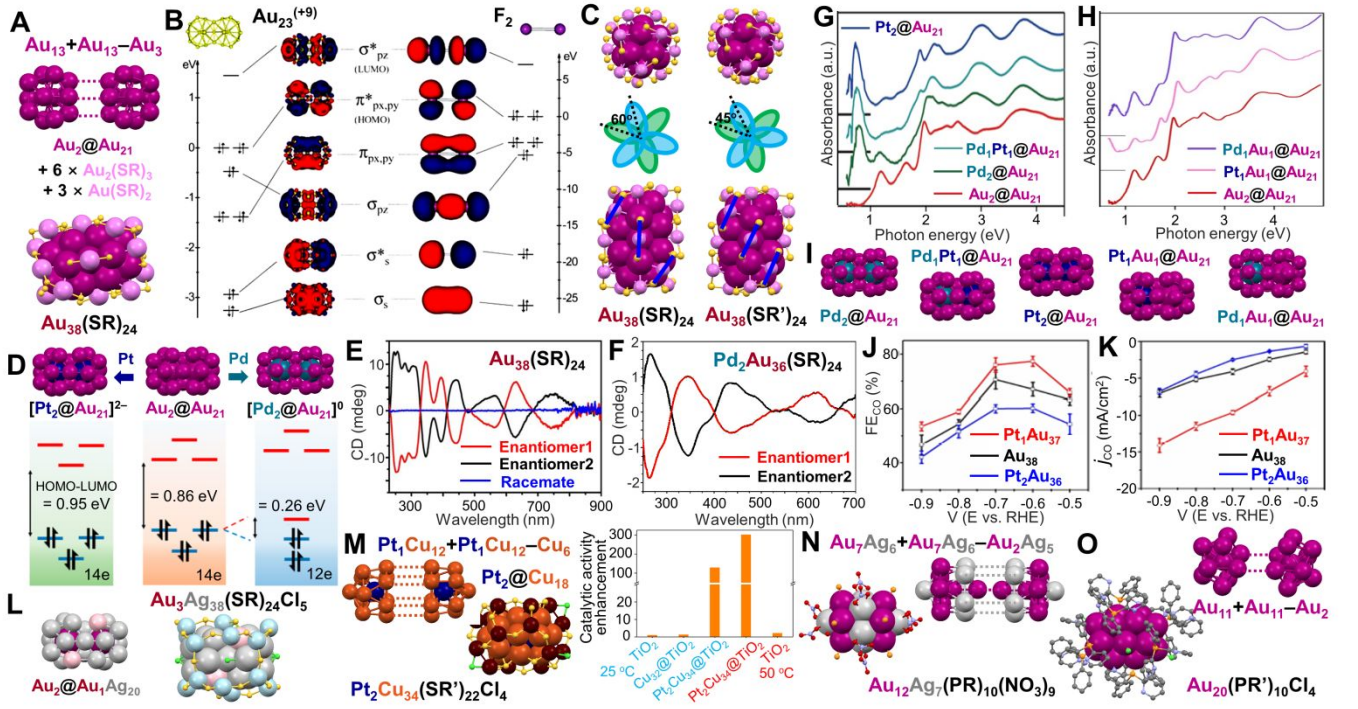

Figure 3. (A) The face-fused $Au_2@Au_{21}$ kernel in $Au_{38}(SR)_{24}$. (B) Comparison of the Kohn–Sham orbital diagrams between $Au_{23}^{(+9)}$ (left) and F_2 (right). Reproduced with permission.[146] Copyright 2013, The Royal Society of Chemistry. (C) Top and front views, and the schematic diagram of two overlapped tri-blade 'fans' of $Au_{38}(SR)_{24}$ (left) and $Au_{38}(SR')_{24}$ (right). Reproduced with permission.[148] Copyright 2020, The Royal Society of Chemistry. (D) DFT-calculated electronic energy levels of $[Pt_2Au_{36}(SCH_3)_{24}]^{2-}$, $Au_{38}(SCH_3)_{24}$, and $[Pd_2Au_{36}(SCH_3)_{24}]^0$. Reproduced with permission.[154] Copyright 2018, American Chemical Society. (E) Circular dichroism spectra of two enantiomers and the racemic $Au_{38}(SR)_{24}$. Reproduced with permission.[121] Copyright 2012, Macmillan Publishers Limited. (F) Circular dichroism spectra of two enantiomers of $Pd_2Au_{36}(SR)_{24}$. Reproduced with permission.[156] Copyright 2014, American Chemical Society. (G) Absorption spectra of $Pt_2Au_{36}(SR)_{24}$, $PdPtAu_{36}(SR)_{24}$, $Pt_2Au_{36}(SR)_{24}$ and $Au_{38}(SR)_{24}$ as a function of photon energy. Reproduced with permission.[157] Copyright 2020 Wiley-VCH GmbH. (H) Absorption spectra of $Pd_1Au_{37}(SR)_{24}$, $Pt_1Au_{37}(SR)_{24}$ and $Au_{38}(SR)_{24}$ as a function of photon energy. Reproduced with permission.[158] Copyright 2022, The Authors. (I) The 23-metal kernels with different dopants. (J) CO Faradaic efficiency and (K) CO partial current density for $Pt_1Au_{37}(SR)_{24}$, $Au_{38}(SR)_{24}$, and $Pt_2Au_{36}(SR)_{24}$ catalysts at different applied potentials. Reproduced with permission.[159] Copyright 2022, Wiley-VCH GmbH. (L) The $Au_2@Au_1Ag_{20}$ kernel of $Au_3Ag_{38}(SR)_{24}X_5$. (M) The $Pt_2@Cu_{18}$ kernel in $Pt_2Cu_{34}(SR')_{22}Cl_4$, and the enhanced catalytic activity of $Pt_2Cu_{34}@TiO_2$ for silane oxidation to silanol. Reproduced with permission.[160] Copyright 2021, American Chemical Society. (N) The fusion of $Au_{12}Ag_7$ core in $Au_{12}Ag_7(PR)_{10}(NO_3)_9$. (O) The fusion of Au_{20} core in $Au_{20}(PR')_{10}Cl_4$. Color codes: magenta/violet = Au, dark cyan = Pd, dark blue = Pt, light grey/light blue = Ag, pink = Au/Ag, orange/brown = Cu, yellow = S, light orange =P, green = Cl, red = O, light purple = N, and grey = C. R groups are omitted or simplified for clarity.

Syntheses other than the original size-focusing method have also been developed to understand the formation of dimeric $Au_{38}(SR)_{24}$ NCs. Maran et al. found that the charge-neutral $Au_{25}(SR)_{18}$ NCs could undergo a spontaneous bimolecular fusion to form the dimeric $Au_{38}(SR)_{24}$ NC during a period of two weeks.[161] The Tuskuda group developed a hydride-mediated transformation approach by reacting equivalent amounts of $[HM_1Au_8(PPh_3)_8]^+$ (8e) and $[M_1Au_{24}(SR)_{18}]^-$ (M = Pd/Pt), resulting in homodimeric $Pd_2Au_{36}(SR)_{24}$ and $Pt_2Au_{36}(SR)_{24}$ as well as heterodimeric $Pd_1Pt_1Au_{36}(SR)_{24}$ with crystal structures solved (Figure 3G), proving that Pd or Pt atoms are doped at the centers of the individual icosahedra. The lowest-energy absorption bands of

$M_2Au_{36}(SR)_{24}$ ($12e^-$) are determined to be ~0.7 eV, and the electron configuration of $(1\Sigma)^2(1\Sigma^*)^2(1\Pi)^4(2\Sigma)^2(1\Pi^*)^2$ corresponds to the O_2 electron configuration.[157] Very recently, the authors modified the method by mixing equivalent $[HAu_9(PPh_3)_8]^{2+}$ (8e) and $[M_1Au_{24}(SR)_{18}]^-$ with excess Au(I)-SR oligomer, and after chromatography separation, heterodimeric $M_1Au_{37}(SR)_{24}$ ($13e^-$) was obtained.[158] The optical absorption spectra of $M_1Au_{37}(SR)_{24}$ show an additional band below 1 eV compared to that of $Au_{38}(SR)_{24}$ (Figure 3H), which can be assigned to the electronic transition to a singly occupied molecular orbital. The 23-metal-atom kernel structures with different dopant(s) are shown in Figure 3I. In the meantime, Y. Zhu et al. independently reported the same $13e^-$ $Pt_1Au_{37}(SR''')_{24}$ NC (SR''' = SCH_2Ph^tBu) by traditional co-reduction and separation methods. More interestingly, $Pt_1Au_{37}(SR''')_{24}$ with an unpaired electron displays a higher catalytic activity than that of $Pt_2Au_{36}(SR''')_{24}$ in electroreduction of CO_2, whereas $Au_{38}(SR''')_{24}$ is in between (Figure 3J/K).[159]

Moreover, $Au_{38}(SR)_{24}$ has a structural isomer, denoted $Au_{38}(SR)_{24}$' which possesses an Au_{23} kernel composed of one I_h Au_{13} and one Au_{12} cap fused together by sharing two Au atoms.[162] Although $Au_{38}(SR)_{24}$' is thermally less stable than the homodimeric $Au_{38}(SR)_{24}$, it shows much higher catalytic activity in reducing 4-nitrophenol to 4-aminophenol at 0 °C.

In addition to the NCs with Au-based bi-I_h kernels, $Au_3Ag_{38}(SR)_{24}X_5$ (X = Cl or Br, SR = SCH_2Ph) with an Ag-based bi-I_h kernel was also reported.[163] The two icosahedrons centrally doped with Au atoms are face-fused into a dimeric $Au_2@Au_1Ag_{20}$ kernel (one Au is distributed at two sites (~50%) on the surface of the kernel, Figure 3L, left), which is further capped by two halogens at two ends and an outer $Ag_{18}(SR)_{24}X_3$ shell (Figure 3L, right). The NC also has the same $14e^-$ configuration as the $Au_{38}(SR)_{24}$ system, and shows an emission peak at 827 nm and a shoulder band at 851 nm in solid state at room temperature. In another work, due to the distinct chemical reactivity of $[Cu_{32}H_8(SR')_{24}Cl_2]^{2-}$ (SR' = SC_2H_4Ph), Hyeon et al. reacted it with $Na_2PtCl_6{\cdot}6H_2O$ under an Ar atmosphere to produce $[Pt_2Cu_{34}(SR')_{22}Cl_4]^{2-}$ ($10e^-$) NCs. Two incomplete I_h Pt_1Cu_{12} units are fused at the Cu_6 hexagon, resulting in a rod-shaped Pt_2Cu_{18} kernel inside a $Cu_{16}(SR')_{22}Cl_4$ shell (Figure 3M). The synergistic effect of the bimetallic NC was found to enhance the catalytic activity by ~300 fold in silane-to-silanol conversion under mild conditions.[160]

For phosphine-protected NCs, when two I_h Au_7Ag_6 units are fused by sharing an Au_2Ag_5 part, $Au_{12}Ag_7(PR)_{10}(NO_3)_9$ (PR = $PPh(CH_3)_2$) with a nearly staggered Au_5–Ag_5–Au_5 configuration is obtained (Figure 3N).[164] Another $Au_{20}(PR')_{10}Cl_4$ NC (PR' = bis(2-pyridyl)phenyl-phosphine) has an Au_{20} core generated from the fusion of two Au_{11} units (incomplete icosahedron) via two sharing vertices (Figure 3O).[165]

The formation of dimeric structures is elusive due to their ultrasmall sizes. But we noticed that many of the dimeric I_h NCs also have their corresponding monomeric I_h structures that can be separately synthesized to have superatomic character. Thus, the formation mechanism of dimeric NCs could be referred to the model of diatomic molecules or fusion growth.

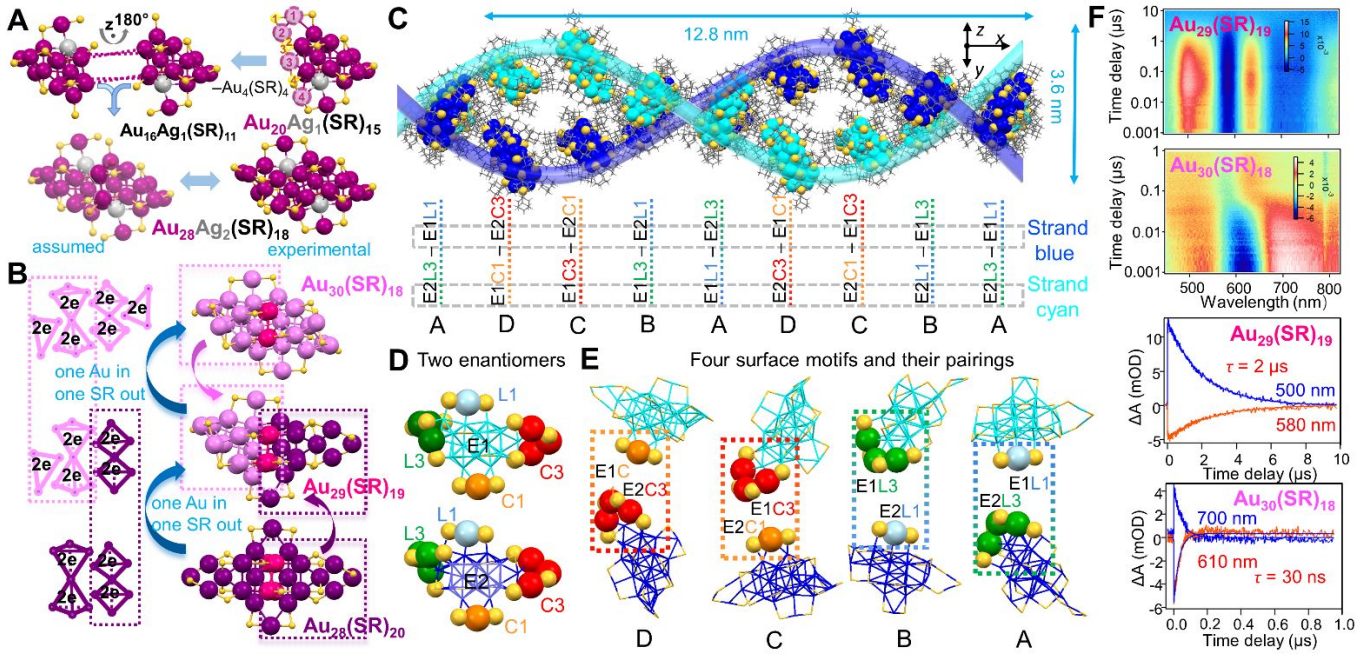

Figure 4. (A) Proposed formation of dimeric $Au_{28}Ag_2(SR)_{18}$. Reproduced with permission.[166] Copyright 2020, American Chemical Society. (B) Geometric and electronic structural evolutions achieved by the 'one gold in, one thiolate out' approach, from $Au_{28}(SR)_{20}$ to $Au_{29}(SR)_{19}$, then to $Au_{30}(SR)_{18}$. Color codes in (A/B): magenta/violet/dark pink/purple = Au, light grey = Ag, yellow = S, R groups are omitted for clarity. (C) Self-assembly of $Au_{29}(SR)_{19}$ NCs into a double-helical structure; (D) two enantiomers (E1 and E2) of $Au_{29}(SR)_{19}$ in the supercrystal; and (E) four types of motifs matching between neighboring enantiomers: E1C1–E2C3 (D type), E1C3–E2C1 (C type), E1L3–E2L1 (B type) and E1L1–E2L3 (A type). Color code in C/D/E: blue and cyan = Au in the different strands; yellow = S; grey = C. The four different staple motifs of $Au_{29}(SR)_{19}$ are marked with larger spheres of different colors. (F) Nanosecond transient absorption data and kinetic traces for $Au_{29}(SR)_{19}$, and $Au_{30}(SR)_{18}$. λ_{ex} = 400 nm. Reproduced with permission.[38] Copyright 2021 Springer Nature Limited.

All the above dimeric structures are formed by two I_h or quasi-I_h units which are easier to be identified. By contrast, understanding the formation of *fcc* nanostructures at the atomic level remains a major task. The Jin group used an atom-tracing strategy by heteroatom doping into $Au_{30}(SR)_{18}$ (SR = S^{t}Bu) to label the specific positions in it, which is consistent with the Ag-doping site in $Au_{20}Ag_1(SR)_{15}$, indicating that the 30-metal-atom NC is a homodimeric structure (Figure 4A). Electronic orbital analysis by DFT also shows the intrinsic orbital localization at the two specific positions in $M_{30}(SR)_{18}$ (M = Au/Ag), regardless of Au or Ag occupancy. The mechanism is proposed as follows: first, $Au_{16}Ag_1(SR)_{11}$ intermediates (its structure proposed from $Au_{20}Ag_1(SR)_{15}$ by losing $Au_4(SR)_4$) are formed at the initial stage; then, two of them are fused in a face-to-face manner; after eliminating another $Au_4(SR)_4$ unit from the adduct, the dimeric $Au_{28}Ag_2(SR)_{18}$ is achieved (Figure 4A).[166]

The homodimeric structure of *fcc* Au NCs has long been overlooked until the report on heterodimeric *fcc* NCs. Before being experimentally proved, Pei et al. proposed in 2017 a "Au insertion, SR elimination" mechanism based on the structures of $Au_{30}(SR)_{18}$ and $Au_{28}(SR)_{20}$, and predicted the atomic structure of $Au_{29}(SR)_{19}$ with $10e^-$.[167] The crystal structure of heterodimeric $Au_{29}(SR)_{19}$ was finally obtained in 2021 by applying adamantanethiol (SR = SC_5H_{10}).[38] Indeed, half of the $Au_{29}(SR)_{19}$ structure is the same as that of $Au_{30}(SR)_{18}$, and the other half is identical to that of $Au_{28}(SR')_{20}$ (SR' = S-*c*-C_6H_{11}) reported before.[168] In addition to their geometric structure relationship, $Au_{29}(SR)_{19}$ is also heterodimeric in terms of its electronic structure ($4e^- + 6e^-$), whereas the two parent homodimeric NCs show $6e^- + 6e^-$ for $Au_{30}(SR)_{18}$, and $4e^- + 4e^-$ for $Au_{28}(SR')_{20}$ (Figure 4B).[38] With respect to the NP assembly behavior, isotropic NPs lacking directional interactions usually adopt basic packing rules in their self-assembly, wheras remarkable physicochemical properties in metallic NPs are usually originated from the symmetry breaking in the particles (i.e., anisotropic NPs). Thus, we are also expecting some special properties resulted from the heterodimeric structure of the atomically precise $Au_{29}(SR)_{19}$ NC. Suprisingly, these heterodimeric $Au_{29}(SR)_{19}$ NCs self-assemble into double- and quadruple-helical superstructures, whereas the homodimeric $Au_{30}(SR)_{18}$ NCs only form layer-by-layer assemblies.[38] Each pitch of the double helix contains 16 NCs (pitch length 12.8 nm and width 3.6 nm), in which 8 NCs in each strand adopt different rotation angles in the assembly (Figure 4C).[38] Moreover, the great advantage of atomically precise nanochemistry is that it reveals how such complex arrangements are formed, while this cannot be achieved in conventional NPs due to imperfections. With atomically precise NCs, two enantiomers (E1 and E2) are identified, and the heterodimeric $Au_{29}(SR)_{19}$ has four types of staple motifs: one monomeric $Au(SR)_2$ motif (denoted L1) and one trimeric $Au_3(SR)_4$ (denoted L3) inherited from $Au_{30}(SR)_{18}$; and one monomeric $Au(SR)_2$ (denoted C1) and one trimeric $Au_3(SR)_4$ (denoted C3) inherited from $Au_{28}(SR)_{20}$ (Figure 4D). When assembling into a supercrystal, the two neighboring enantiomers approach each other by matching their C1 and C3 staple motifs, or their L1 and L3 staple motifs (Figure 4E), resulting in four types of interactions: E1C1–E2C3 (denoted D), E1C3–E2C1 (denoted C), E1L3–E2L1 (denoted B) and E1L1–E2L3 (denoted A).[38] Specifically, when the C1 and C3 staple motifs of two enantiomers pair up (Figure 4E, via D and C interactions), the ligands surrounding them are triply paired (resembling base pairing of C and G); when the L1 and L3 staple motifs of two enantiomers pair up (Figure 4E, via B and A interactions), the ligands surrounding them are doubly paired (resembling base paring of A and T). It is noteworthy that the helical assembly is driven by van der Waals interactions through particle rotation and conformational matching, as opposed to hydrogen-bonding and π-π stacking in DNA. Furthermore, the heterodimeric $Au_{29}(SR)_{19}$ has a photoexcited carrier lifetime that is ~65 times longer than that of the homodimeric $Au_{30}(SR)_{18}$ (Figure 4F), resulting in the NIR photoluminescence in $Au_{29}(SR)_{19}$ (see scheme 1).[38] An $Au_{29}(SAdm)_{19}$ film in which nanoclusters are randomly packed enhances the photoluminescence by suppressing non-radiative decays. Supercrystals in which nanoclusters are self-assembled into double-helixes lead to further photoluminescence enhancement, arising from the collective properties of assembly and ordered anisotropic interactions.[38]

Additionally, M. Zhu et al. reported a halogen-induced anisotropic growth of $Ag_{40}(C_6H_5COO)_{13}(SR)_{19}(CH_3CN)$ into $Ag_{45}(C_6H_5COO)_{13}(SR)_{22}Cl_2$ (SR = SCH_2Ph^tBu), in which the adsorption of halogen ions might lead to the formation of defected intermediates for epitaxial growth at both ends of the kernel.[169] In another work, $Ag_{48}Cl_{14}(SR')_{30}$ and $Ag_{50}Cl_{16}(SR')_{28}(dppp)_2$ (SR' = SC_5H_{10}, dppp = $Ph_2P(CH_2)_3PPh_2$) share the same framework containing a prolate Ag_8 kernel (an Ag_6 octahedron with two polar Ag atoms), except that the $Ag_2(SR')_3$ active units at the two ends of $Ag_{48}Cl_{14}(SR')_{30}$ are replaced with $Ag_3(SR')_2(dppp)Cl$ units in $Ag_{50}Cl_{16}(SR')_{28}(dppp)_2$ with a more anisotropic shape.[170] In $Au_7Cu_{12}(PR)_6(SR'')_6Br_4$ (PR = diphenylphosphinopyridine, SR'' = SPh^{t}Bu), the central Au is capped by an Au_3Cu_3 ring and further by a Cu_3 motif from either side. The bimetallic NC demonstrates strong emission with 13.2% quantum yield (QY), which can be further improved by exchanging the aromatic thiolates with non-aromatic ones to break the intramolecular $\pi\cdots\pi$ interactions.[171]

Jin et al. also introduced a Cd–Br bond into Au NCs, resulting in bimetallic $Au_{22}Cd_1(SR)_{15}Br$ (see Scheme 1), and trimetallic $Au_{22-x}Ag_xCd_1(SR)_{15}Br$ (avg. x = 1.87, SR = SC_5H_{10}). Half of the I_h Au_{13} or $Au_{13-x}Ag_x$ kernel is capped by three $Au_3(SR)_4$ motifs, whereas the other half has only a $(SR)_3CdBr$ motif on it. Due to the presence of the special Cd–Br on the surface, the NC with metal core radius of 5 Å shows giant dipoles (~18 D), falling in the experimental trend of II–VI quantum dots. The strong dipole–dipole interactions lead to a "head-to-tail" alignment of the $Au_{22-x}Ag_xCd_1(SR)_{15}Br$ NCs in the crystalline state.[122] In another case resulted from surface reconstruction due to doping, the cuboctahedral Au_{13} kernel is capped by two $Cd_3[Au(SR')_2]_3$ (SR' = S-*c*-C_6H_{11}) motifs on each side, resulting in a $Au_{19}Cd_2(SR')_{15}$ NC.[172] Compared to $Au_{23}(SR')_{15}$ prior to surface reconstruction, the Cd-substituted NC greatly enhances the CO_2 electroreduction selectivity to 90–95% at applied potential between -0.5 to -0.9 V vs RHE.[173]

Rod-shaped nanoclusters

The Konishi group has done extensive works on diphosphine coordinated [core+*exo*]-type Au NCs (nuclearity = 6, 7, 8, and 11) featuring a polyhedral core with *exo* one or two gold atom(s),[174–176] resembling ultrasmall Au nanorods. The $Au_6(dppp)_4$, $Au_8(dppp)_4Cl_2$, and $Au_{11}(dppe)_6$ solutions (dppp = $Ph_2P(CH_2)_3PPh_2$, dppe = $Ph_2P(CH_2)_2PPh_2$) show vivid colors corresponding to the intense single band for each NC in the visible region, well-separated from the absorption at higher energy (Figure 5A).[129] By contrast, the core-only isomers of the same nuclearity show overlapped bands from UV to visible region. DFT calculations revealed that the *exo* Au atoms are highly involved in the frontier molecular orbitals and HOMO–LUMO transition, giving rise to the isolated characteristic single absorption of the [core+*exo*]-type Au NCs.[177] By replacing dppp with dppmb (dppmb = Ph_2P-Ph-PPh_2), $Au_6(dppmb)_4$ has its Au_6 framework proximate to the phenylene bridges, and hydrogen bonding interaction can be identified and a large red shift (45 nm) of the visible absorption band is observed by spectroscopy.[178]

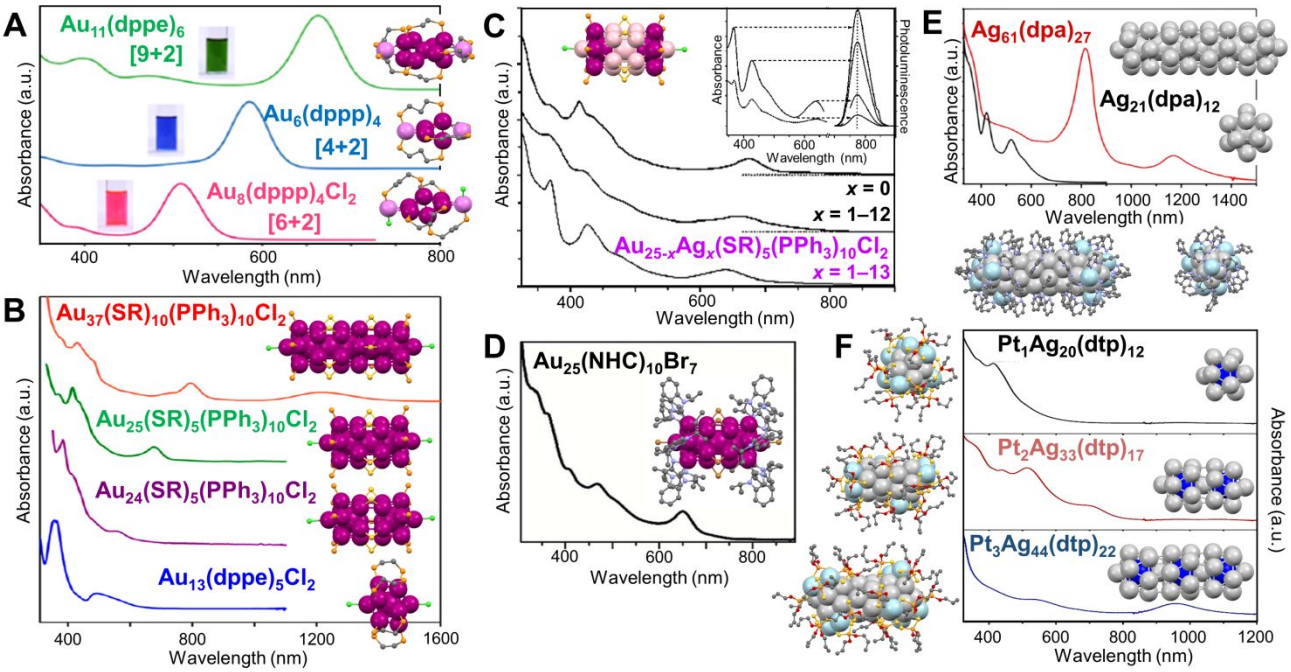

Figure 5. (A) Absorption spectra of $Au_6(dppp)_4$, $Au_8(dppp)_4Cl_2$, $Au_{11}(dppe)_6$, and corresponding structures. Reproduced with permission.[129] Copyright 2013, American Chemical Society. (B) Absorption spectra of $Au_{37}(SR)_{10}(PPh3)_{10}Cl_2$, $Au_{25}(SR)_5(PPh_3)_{10}Cl_2$, $Au_{24}(SR)_5(PPh_3)_{10}Cl_2$, $Au_{13}(dppe)_5Cl_2$, and corresponding structures. Reproduced with permission.[130] Copyright 2017, The Authors, published by National Academy of Sciences. (C) Absorption spectra of $Au_{25-x}Ag_x(SR)_5(PPh_3)_{10}Cl_2$ (x = 0, 1–12, or 1–13), and corresponding structure. Inset, absorption and excitation spectra (left), and emission spectrum (right) at different excitation wavelengths. Reproduced with permission.[179] Copyright 2014, Wiley-VCH GmbH. (D) Absorption spectra of $Au_{25}(NHC)_{10}Br_7$, and corresponding structure. Reproduced with permission.[180] Copyright 2019, Wiley-VCH GmbH. (E) Optical absorption spectra of $Ag_{61}(dpa)_{27}$ and $Ag_{21}(dpa)_{12}$ NCs, and corresponding total structures and I_h cores. Reproduced with permission.[181] Copyright 2021, American Chemical Society. (F) Optical absorption spectra of $Pt_1Ag_{20}(dtp)_{12}$, $Pt_2Ag_{33}(dtp)_{17}$, $Pt_3Ag_{44}(dtp)_{22}$, and corresponding total structures and I_h cores. Reproduced with permission.[182] Copyright 2019, American Chemical Society. Color labels: magenta/violet = Au, pink = Au/Ag, light gray/light blue = Ag, blue = Pt, yellow = S, light orange = P, green = Cl, brown = Br, purple = N, red = O, grey = C. R groups are omitted or simplified for clarity.

Using bimetallic I_h building blocks to constitute cluster of clusters was reported by the Teo group in 1980s, and the M_{13} (M = Au/Ag) units are connected by vertex sharing.[183–185] In 2005, when thiolate was introduced to the solution of $Au_{11}(PPh_3)_8Cl_2$, $Au_{25}(SR)_5(PPh_3)_{10}Cl_2$ (SR = SC_nH_{2n+1}, n = 2-18) NCs with two vertex-sharing I_h Au_{13} units (aspect ratio of 2.3) was produced.[186,187] Later, the Jin group reported another bi-I_h $Au_{24}(SR)_5(PPh_3)_{10}Cl_2$ NC (Figure 5B, purple line) with the shared vertex eliminated by adding excess PPh_3, which is in contrast to the 25-metal-atom rod counterpart (Figure 5B, green line). DFT calculations indicate that the broad band at ~560 nm arises from the HOMO-1 to LUMO+2 transition.[141] Excitingly, a tri-I_h $Au_{37}(SR)_{10}(PPh_3)_{10}X_2$ (X = Cl/Br) with AR = 3.5 was prepared by reducing $Au^I(PPh_3)X$ to clusters, then etching the clusters with excess thiol (Figure 5B, red line).[188] Along with the $Au_{13}(dppe)_5Cl_2$ NC (Figure 5B, blue line) with a mono-I_h core reported by Konishi and coworkers in 2010,[189] the first rod-shaped series of Au NCs is achieved, and the mono-I_h, bi-I_h, and tri-I_h NCs possess $8e^-$, $16e^-$, and $24e^-$, respectively, according to Mingo's electron-counting rule.[190] Moreover, the series shows an interesting trend in the optical absorption spectra (Figure 5B): the high-energy peaks are similar for the series of NCs since the electronic transitions occur within the individual Au_{13};[130,191] whereas the features of dimerization or trimerization due to the interaction between neighboring Au_{13} units are reflected in the red-shifted peaks in visible range.[32] It is noteworthy that the peak significantly shifts to 1230 nm for tri-I_h Au_{37} due to the trimeric interaction (Figure 5B, red line). Moreover, an excited-state exciton localization was observed in the Au_{37} NC which exhibits strong coupling between Au_{13} units after photoexcitation, and kinetic traces indicate the existence of both radial and axial vibration modes.[130] Femtosecond spectroscopic investigations on $Au_{25}(SR)_5(PPh_3)_{10}Cl_2$ show overlapped excited state absorption

and ground state bleach signals. The 0.8 ps component of the lifetime is attributed to the fast internal conversion process from LUMO+n to LUMO, whereas the 2.4 μs long component is due to electron relaxation to the ground state.[192]

The interesting stories of rod-shaped Au_{25} are also highlighted by heteroatom doping. Wang et al. continued to illustrate that substituting Au with Ag not only changed the absorption profile (Figure 5C), but also drastically enhanced the photoluminescence (PL) to as high as QY = 40.1% for $Au_{25-x}Ag_x(SR)_5(PPh_3)_{10}Cl_2$ (x = 1–13, Figure 5C, inset),[179] in striking contrast to the weakly luminescent species (x = 1–12, QY = 0.21%) and the homogold counterpart.[193] In other words, the 13th Ag atom is critical in enhancing PL. Based on the highly photoluminescent rod-shaped $Au_{25-x}Ag_x(SR)_5(PPh_3)_{10}Cl_2$, the self-annihilation electrogenerated chemiluminescence (ECL) was found to be 10 times higher than the standard tris(bipyridine)-ruthenium(II) complex, and co-reactant (tripropylamine) ECL was about 400 times stronger.[194]

By replacing the 10 phosphine ligands with N-heterocyclic carbene ligands and the 5 thiolates with halides, a rod-shaped $Au_{25}(NHC)_{10}Br_7$ NC (NHC = 1,3-diisopropylbenzimidazolin-2-ylidene) was resulted, showing the first absorption peak at ~650 nm, similar to the case of $Au_{25}(SR)_5(PPh_3)_{10}Cl_2$ (Figure 5D). The high thermal and air stabilities of this NC are ascribed to the stronger Au-carbene bond than the Au-phosphine bond (difference up to 0.9 eV) as indicated by DFT. The NC also shows high catalytic activity in homogenous cycloisomerization of alkynyl amines to indoles compared to the trace activity of $Au_{25}(SR)_5(PPh_3)_{10}Cl_2$.[180] With the presence of Pd^{2+}, the assembly of two I_h Pd@Au_{12} units into rod-shaped $Pd_2Au_{23}(PPh_3)_{10}Br_7$ was also achieved.[195] Hetero-bi-I_h $Pd_1Au_{24}(SR)_5(PPh_3)_{10}Cl_2$, i.e., only one I_h unit is central-doped with Pd, was synthesized by etching the crude product (made by co-reducing AuCl(PPh_3) and Pd(PPh_3)$_4$) with thiols in refluxing chloroform.[196] Compared to the rod-shaped Au_{25} NCs, obtaining the rod-shaped Ag_{25} NC (i.e., the silver counterpart) of the same structure is challenging. However, Pt or Pd doping at the centers of the two I_h units could improve the stability of the NCs, resulting in $M_2Ag_{23}(PPh_3)_{10}Cl_7$ (M = Pt/Pd).[197,198]

Very recently, the first supercluster with four I_h Ag_{13} units linearly connected was reported by Q.-M. Wang and Xu.[181] The resulted $Ag_{61}(dpa)_{27}$ (dpa = dipyridylamine) was produced by reducing Ag^I–dpa in the presence of bidentate phosphine, $AgSbF_6$, and CH_3ONa in dichloromethane. The 30e$^-$ of Ag_{61} makes it isolobal to the linear tetraiodide anion I_4^{2-}.[199] Compared with $Ag_{21}(dpa)_{12}$ of which the large energy gap is mainly decided by the superatomic Ag_{13}^{5+} (8e$^-$) unit,[200] $Ag_{61}(dpa)_{27}$ with AR = 4.2 shows an intense absorption peak extending into NIR (819 nm) and the first absorption band at 1170 nm (Figure 5E).[181] The authors attributed the loss of the optical features of mono-I_h Ag_{21} in the spectrum of tetra-I_h Ag_{61} to the stronger electron couplings between the I_h Ag_{13} units, in contrast to the case of Au_{13} vs. Au_{37} (Figure 5B). Besides, with the help of Pt doping, Liu et. al. reported another series of NCs containing one, two or three I_h Pt_1@Ag_{12} units (Figure 5F) by co-reducing Ag^I and Pt^{II} with $LiBH_4$ and chromatography separation. Similar to the Au series, the lowest-energy absorption bands of the Ag series display a red-shift from 412 nm in mono-I_h $Pt_1Ag_{20}(dtp)_{12}$ to 710 nm in bi-I_h $Pt_2Ag_{33}(dtp)_{17}$, then to 956 nm in tri-I_h $Pt_3Ag_{44}(dtp)_{22}$ (dtp: dipropyl dithiophosphate). Although the first two alloy NCs follow the superatomic electron counts of 8e$^-$ and 16e$^-$, respectively, the tri-I_h NC bears only 22e$^-$, representing the first case in NCs that is isoelectric to linear triiodide anion I_3^-.[182] Note that in heteroleptic rod-shaped 25-metal or 37-metal NCs,[82,187,188,196–198] the two or three M_{13} (M = Au/Ag) units are aligned in an eclipsed conformation; whereas in the homoleptic rod-shaped Pt_2Ag_{33}, Pt_3Ag_{44} as well as Ag_{61} NCs,[181,182] a gauche rotational conformation is adopted in the connection of multiple I_h units.

Compared to the rod-shaped NCs composed of more commonly observed I_h units, anisotropic growth of *fcc* structures into nanorods (bulk Au also adopts *fcc* packing) was also reported for Au NCs of atomic precision. It was surprising when an *fcc* kernel was first discovered in $Au_{36}(SR)_{24}$ (SR = SPh^{t}Bu) in 2012.[79] The close-packed atomic planes show an *a*–*b*–*c*–*a* stacking sequence (Figure 6A), resulting in the cubic and cuboid shapes of NCs of *fcc* structures. The numbers indicate how many metal atoms are in each (001) layer. After continuous successes in synthesizing and characterizing $Au_{28}(SR)_{20}$,[80] and $Au_{52}(SR)_{32}$,[87] the Jin group completed a magic series with a unified formular of $Au_{8n+4}(SR)_{2n+8}$ (n = 3–6) in 2016 thanks for the structural determination of $Au_{44}(SR)_{28}$.[201] The progression of NCs from small to large is neatly shown in the mass spectra of the four NCs (Figure 6B). In a concise layer-by-layer mode, all six surfaces of the series of NCs are exclusively terminated by {100} facets, and the anisotropic growth of the magic series can be viewed as subsequently adding an additional 8-gold-atom (001) layer along the *z* direction, with n representing the number of (001) layers (Figure 6A). That is, n = 3 for $Au_{28}(SR)_{20}$, n = 4 for $Au_{36}(SR)_{24}$, n = 5 for $Au_{44}(SR)_{28}$, and n = 6 for $Au_{52}(SR)_{32}$.[201] In 2019, Wu et al. reported that a half (001) layer composed of 4 Au atoms could also be stacked on the full 8-gold-atom (001) layer, resulting in $Au_{56}(SR)_{34}$.[125] Both works show the evolution of optical properties, which is indicated by red-shift of the lowest energy peak (assigned to sp → sp transition) as the kernel grows, and their optical energy gaps are estimated to be 1.76, 1.75, 1.50, 1.39, and 1.30 eV, respectively (Figure 6C, from Au_{28} to Au_{56}). Based on the observation of a top half layer, the theoretical structures of $Au_{32}(SH)_{22}$, $Au_{40}(SH)_{26}$, and $Au_{48}(SH)_{30}$ are predicted as well.[202] Additionally, when the (001) layers composed of 6 Au atoms and 8 Au atoms are stacked alternatively (total 6 layers), another $Au_{42}(SR)_{26}$ NC can be obtained (Figure 6A).[203]

In the meantime that the *fcc* magic series was achieved, the Tsukuda group also synthesized a water soluble $Au_{76}(SR)_{44}$ NC (SR = $SC_2H_4PhCOOH$) by slow reduction,[204] and the powder X-ray diffraction indicated a *fcc* kernel structure elongated along the {100} direction (Figure 6D). Interestingly, the proposed rod-shaped *fcc* Au_{76} NC exhibited a strong NIR absorption band centered at 1340 nm with molar absorption coefficient ε of 3×10^5 $M^{-1}cm^{-1}$ (Figure 6E), much larger than that of the coefficient of HOMO–LUMO transition in most of other gold-thiolate NCs (~1×10^4 $M^{-1}cm^{-1}$).[19] The large value of ε was tentatively ascribed to the large electronic-transition moment arising from the one-dimensional structure.[204] Since $Au_{76}(SR)_{44}$ could be fitted in the $Au_{8n+4}(SR)_{2n+8}$ series with n = 8, theoretical calculations were conducted to predict its structure. Zeng et al. found highly negative values of the nucleus-independent chemical shift in the tetrahedral Au_4 units, explaining the overall stability of the series of *fcc* NCs, and the structures of $Au_{60}(SR)_{36}$, $Au_{68}(SR)_{40}$, and $Au_{76}(SR)_{44}$ were simulated (Figure 6E inset and Figure 6F). Infinite extending of the lattice showed a band gap of 0.78 eV for the gold-thiolate nanowire.[205] At the same time, the Pei group also obtained the same simulated

structure of $Au_{76}(SR)_{44}$ and assigned its NIR absorption to the anisotropic Au kernel which enhanced the longitudinal orbital transition and the ligand passivation, resulting in the red shift of the absorption peak.[206] In another *fcc* NC, Au–Cl–Au motif was first observed in $Au_{36}(SR)_8Cl_{20}$ (SR = SCH_2Ph^tBu), and the total NC can be regarded as four stacking layers in *a*–*b*–*c*–*a* sequence (Figure 6G).[207]

In 2013, Zheng et al. reported a cubic *fcc* Ag building block —$Ag_{14}(SR)_{12}(PPh_3)_8$ (SR = $SPhF_2$) NC.[208] Later, by stacking multiple of such building blocks together, a series of cuboid *fcc* Ag NCs were achieved with six faces and twelve edges capped by thiolates and eight corners terminated by phosphine ligands. In the $Ag_{23}(SR')_{18}(PPh_3)_8$ (SR' = SC_2H_4Ph), its structure is a combination of two cubic units with some twist along the C_2 axis, endowing chirality to the NC (Figure 6H).[209] $Ag_{38}(SR)_{26}(PR')_8$ (PR' = tributylphosphine) is composed of four of such cubes, and its optical spectrum shows three peaks at 413, 507, 563 nm, with some weak absorption bands as well (Figure 6I),[210] while the Ag_{14} building block NC only shows two shoulder bands.[208] Linear-response time-dependent DFT indicates that the Ag_{38} is rather electronically stable, with an energy gap of 0.67 eV. A larger cubic $Ag_{63}(SR)_{38}(PR')_8$ of 2×2×2 size was also reported in the same work and a theoretical 3×3×3 $Ag_{172}(SR)_{72}(PR')_8$ was predicted.[210] Additionally, the Bakr group revealed an Ag NC built up with 12 units, i.e., $Ag_{67}(SR'')_{32}(PPh_3)_8$ (SR'' = $SPh(CH_3)_2$). Its UV-vis spectrum shows similar strong absorption between 400 to 600 nm as $Ag_{38}(SR)_{26}(PR')_8$, but with an additional peak at ~680 nm (Figure 6J).[211]

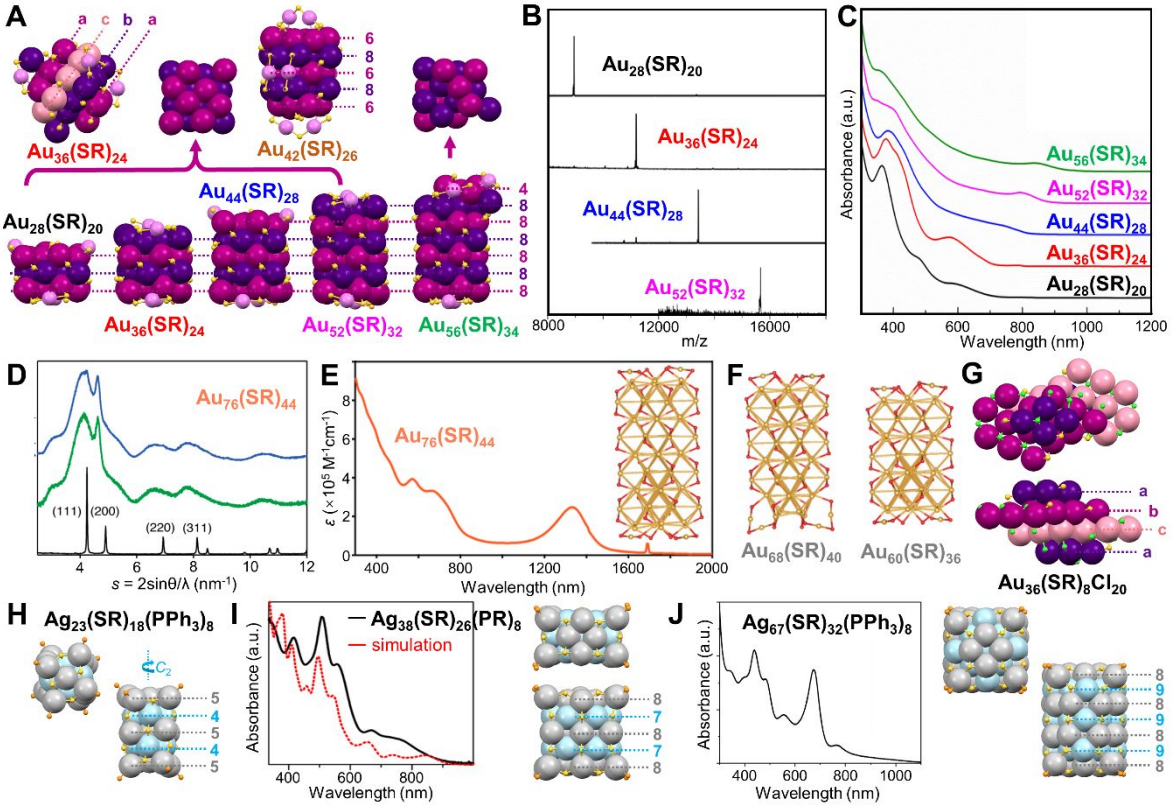

Figure 6. (A) The anisotropic growth of the *fcc* lattice of $Au_{28}(SR)_{20}$, $Au_{36}(SR)_{24}$, $Au_{44}(SR)_{28}$, $Au_{52}(SR)_{32}$, and $Au_{56}(SR)_{34}$ NCs with top views of the $Au_{8n+4}(SR)_{4n+8}$ magic series compared to $Au_{56}(SR)_{34}$, and the structure of $Au_{42}(SR)_{26}$. (B) ESI-MS spectra of the $Au_{8n+4}(SR)_{4n+8}$ series, n = 3–6. The m/z = $[Au_n(SR)_m+Cs]^+$. Reproduced with permission.[201] Copyright 2016, American Chemical Society. (C) Absorption spectra of the *fcc* series. Reproduced with permission.[125] Copyright 2020, Wiley-VCH GmbH. (D) Powder XRD patterns of $Au_{76}(SR)_{44}$ before (green) and after (blue) amidation reaction, and bulk gold (black). (E) UV–vis–NIR absorption spectrum of $Au_{76}(SR)_{44}$ solution. Reproduced with permission.[204] Copyright 2015, American Chemical Society. (F) The optimized theoretical structures of $Au_{60}(SR)_{36}$, $Au_{68}(SR)_{40}$, and $Au_{76}(SR)_{44}$. Reproduced with permission.[205] Copyright 2016, The Royal Society of Chemistry. (G) Top and side views of $Au_{36}(SR)_8Cl_{20}$. (H) Top and side views of $Ag_{23}(SR)_{18}(PPh_3)_8$. (I) Experimental and calculated absorption spectra of $Ag_{38}(SR)_{26}(PR)_8$, and corresponding top and side views of the structure. Reproduced with permission.[210] Copyright 2016, American Chemical Society. (J) Absorption spectra of $Ag_{67}(SR)_{32}(PPh_3)_8$, and corresponding top and side views of the structure. Reproduced with permission.[211] Copyright 2016, American Chemical Society. Color codes: magenta/purple/pink/violet = Au, light grey/light blue = Ag, yellow = S, green = Cl, light orange = P. R groups are omitted for clarity.

So far, NCs with I_h, *fcc*, or decahedral kernels constitute the majority of atomically precise noble metal NCs.[32,48,212–214] By comparison, Au NCs with hexagonal-close-packed (*hcp*) kernels are very rare, and no *hcp* structure is ever found in any Ag NCs. We start from $Au_{24}(SR)_{20}$, although it does not have an *hcp* kernel. Based on the formular of $Au_{24}(SR)_{20}$ obtained in experiment,[215] two isomeric structures with low energies were predicted by Pei et al. in 2011,[216] and both of them were proved by crystallography later. The total structure of $Au_{24}(SR)_{20}$ was first solved by applying SR = SCH_2Ph^tBu.[82] Two tetrahedral Au_4 units are joined at their triangle faces by 60° rotation to form a bi-tetrahedral Au_8 kernel. One pair of $Au_4(SR)_5$ staples is assembled onto the two ends of the Au_8 kernel via bi-dentate bonding; and a second pair of the tetrameric staples is further attached to the Au_8 kernel by rotating ~90° relative to the first pair (Figure 7A, inset). Other thiols were also used to prepare

the same 24-gold-atom NC, and the fluorescence QY decreased from 2% for $Au_{24}(SCH_2Ph^tBu)_{20}$, to 1.5% for $Au_{24}(SCH_2Ph)_{20}$, then to 0.3% for $Au_{24}(SC_2H_4Ph)_{20}$, with the emission peak slightly blue-shifted (Figure 7B/7C), correspondence to the electron-donor strength of the ligand.[126] By contrast, selenolate-protected $Au_{24}(SePh)_{20}$ shows an isomeric structure in which two tetrahedral Au_4 units cross-join together at the edges (rather than the faces), and the new Au_8 kernel is protected by a pair of $Au_5(SePh)_6$ motifs as well as a pair of $Au_3(SePh)_4$ motifs (Figure 7D, left).[217] The $Au_{24}(SePh)_{20}$ NC is not luminescent in the detective range (Figure 7B/7C).[126] In another case, the Au_9 kernel of $Au_{18}(SR)_{14}$ (SR = S-*c*-C_6H_{11}) can be viewed as three Au_3 layers arranged in an *a*–*b*–*a* manner (Figure 7D, middle),[218,219] and the middle Au_3 layer can be replaced by an Ag_3 layer without changing the structure.[220] It is until the report of $Au_{30}(SR)_{18}$ (SR = adamantanethiolate, SC_5H_{10}) that a complete *hcp* kernel was identified since four layers of Au_3–Au_6–Au_6–Au_3 are packed in an *a*–*b*–*a*–*b* manner, and the total structure has an unprecedentedly high S_6 symmetry (Figure 7D, right), resulting in the special solubility of the NC, i.e., only soluble in benzene.[221]

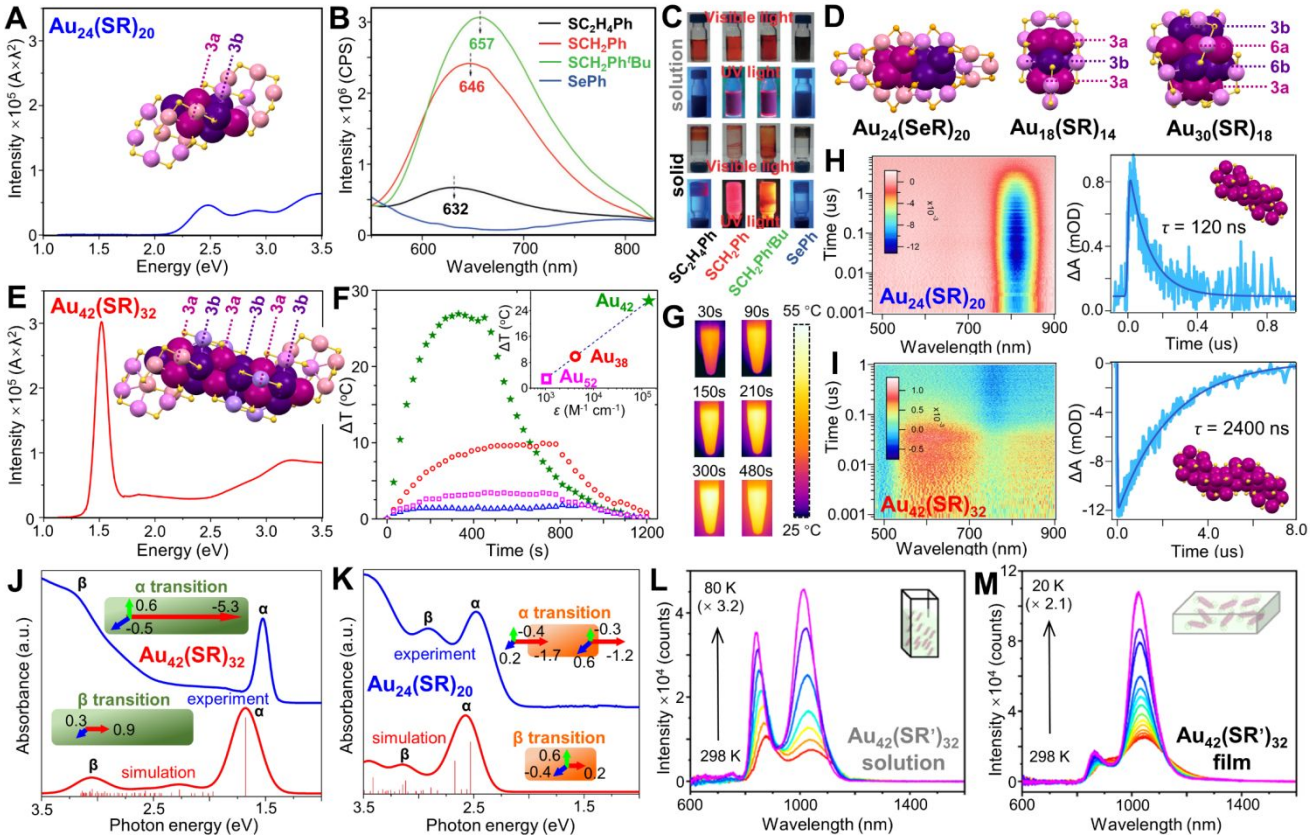

Figure 7. (A) Absorption spectra (photon energy scale) of $Au_{24}(SR)_{20}$ with corresponding structures shown in the insets. (B) Fluorescence spectra of $Au_{24}(SR)_{20}$ NCs with different thiolate ligands and $Au_{24}(SeR)_{20}$ NCs in CH_2Cl_2, and (C) digital photographs of samples in solution or solid states under visible and 365 nm UV light irradiation. Reproduced with permission.[126] Copyright 2016, Wiley-VCH GmbH. (D) Structures of $Au_{24}(SeR)_{20}$, $Au_{18}(SR)_{14}$ and $Au_{30}(SR)_{18}$. (E) Absorption spectra (photon energy scale) of $Au_{42}(SR)_{32}$ with corresponding structures shown in the insets. (F) Temperature changes of $Au_{42}(SR)_{32}$, $Au_{38}(SR)_{24}$, $Au_{52}(SR)_{32}$, and $Au_{24}(SR)_{20}$ in toluene (50 μg mL^{-1}) upon irradiation at 808 nm, 1 W cm^{-2}, inset: the relationship between ΔT and molar absorption coefficient of NC solutions at irradiation wavelength. (G) Time-dependent images of $Au_{42}(SR)_{32}$ solution upon irradiation. (H) ns-TA data map of $Au_{24}(SR)_{20}$ and its TA kinetic traces and fitting (probed at 580 nm). (I) ns-TA data map of $Au_{42}(SR)_{32}$ and its TA kinetic traces and fitting (probed at 813 nm). λ_{ex} = 400 nm. (J) Experimental absorption spectra (blue) and TDDFT-simulated absorption spectra (red) of (J) $Au_{42}(SR)_{32}$ and (K) $Au_{24}(SR)_{20}$, insets, schematic illustrations of α and β electronic transitions. (A, E-K) Reproduced with permission.[127] Copyright 2022, American Chemical Society. Temperature-dependent PL spectra of (L) $Au_{42}(SR')_{32}$ in 2-methyletetrahydrofuran, and (M) $Au_{42}(SR')_{32}$/PS film. Reproduced with permission.[128] Copyright 2022, American Chemical Society. Color codes: magenta/purple = kernel Au, violet/pink = motif Au, yellow = S, light orange = Se. Organic ligands are omitted for clarity.

A new breakthrough was achieved when the total structure of a rod-shaped $Au_{42}(SR)_{32}$ (SR = SCH_2Ph) NC with a long *hcp* kernel was resolved very recently.[127] When comparing the optical absorption spectra, the lowest energy absorption peak of $Au_{24}(SR)_{20}$ is at 2.5 eV (Figure 7A), whereas that of $Au_{42}(SR)_{32}$ red-shifts to 1.5 eV (Figure 7E) with 6.5 times stronger intensity. The *hcp* Au_{20} kernel of $Au_{42}(SR)_{32}$ comprises six Au_3 layers with two capping Au atoms on opposite ends of the rod, i.e., Au_1–Au_3–Au_3–Au_3–Au_3–Au_3–Au_3–Au_1, compared to the Au_8 kernel (Au_1–Au_3–Au_3–Au_1) in $Au_{24}(SR)_{20}$. Two pairs of $Au_4(SR)_5$ staples are attached to the two ends of the Au_{20} kernel, similar to what is observed in $Au_{24}(SR)_{20}$, but the much longer kernel further requires six short $Au(SR)_2$ motifs to protect its body (Figure 7E, inset). The aspect ratio of the long *hcp* Au_{20} kernel is as large as 6.2, providing a great opportunity to study new properties, since the confinement of excitons within the long but narrow kernel leads to strong photothermal conversion upon photoexcitation. The molar absorption coefficient ε of $Au_{42}(SR)_{32}$ is 1.4×10^5 M^{-1} cm^{-1} at 815 nm, and upon 808 nm excitation (the most commonly used laser for photothermal

therapy with minimum extinction by human tissues),[222,223] very rapid heating was observed as the temperature change (ΔT) reached ~27 °C within only ~5 min (Figure 7F, green stars/7G).[127] By comparison, other anisotropic Au-SR NCs, including $Au_{38}(SR)_{24}$ with dimeric Au_{23} kernel (see Figure 3A), and $Au_{52}(SR)_{32}$ with a layer-by-layer *fcc* Au_{48} kernel (see Figure 6A), increased only by ~10 and ~3 °C, respectively (Figure 7F, red circles and magenta squares). ΔT is almost linear with respect to the exponential scale of ε at the irradiation wavelength. In transient absorption (TA) analysis, although almost the same fast decay was observed in both $Au_{42}(SR)_{32}$ and $Au_{24}(SR)_{20}$ (long and short rods), the nanosecond TA showed the decay lifetimes (τ) of $Au_{24}(SR)_{20}$ was 120 ns (Figure 7H), much shorter than the 2400 ns of $Au_{42}(SR)_{32}$ (Figure 7I). Moreover, TDDFT calculations (Figure 7J) found that the transition dipole moment of peak α (corresponding to HOMO to LUMO transition) of $Au_{42}(SCH_3)_{32}$ is ~10 times stronger along the longitudinal transition than along the transverse transition, indicating the strong NIR absorption is a longitudinal transition, reminiscent of the NIR band of plasmonic Au nanorods. It is a surprise to see that longitudinal excitation can be inherited by NCs of molecular state. For $Au_{24}(SCH_3)_{20}$ with a much shorter kernel, the longitudinal transition of the first peak is not as strong as the case of $Au_{42}(SCH_3)_{20}$, but still stronger than the transverse transitions (Figure 7K).[127]

In addition to the unprecedented photothermal conversion properties, a photoluminescence study on the same $Au_{42}(SR')_{32}$ NC (SR' = SC_2H_4Ph) found a dual NIR emission at 875 and 1040 nm, corresponding to fluorescence and phosphorescence, respectively (Figure 7L). The QY of $Au_{42}(SR')_{32}$ was measured to be 11.9% in ambient CH_2Cl_2 solution at room temperature. Furthermore, when the NCs were embedded in polystyrene (PS) films (solid state), the fluorescence was dramatically suppressed while the phosphorescence was significantly enhanced (Figure 7M), which was ascribed to the largely enhanced intersystem crossing from singlet to triplet excited state induced by dipolar interaction.[128] On a note, Wu et al. independently reported the same $Au_{42}(SR)_{32}$ NC obtained by a thermal and ligand exchange induced *fcc*-to-*hcp* structural transformation, and time-dependent DFT was performed to interpret the Au_{42} dual emission.[224]

Finally, some clues can be drawn from the synthesis to understand how the ultrasmall $Au_{42}(SR)_{32}$ nanorod was achieved. In the synthesis reported by the Jin group,[127] $Au_{42}(SR)_{32}$ was separated from $Au_{24}(SR)_{20}$ by thin layer chromatography, and the as-synthesized mixture of NCs also contains $Au_{25}(SR)_{18}$ and $Au_{38}(SR)_{24}$. Since $Au_{38}(SR)_{24}$ is a dimeric structure of two $Au_{25}(SR)_{18}$ through fusion (see Figure 3 and discussion therein), $Au_{42}(SR)_{32}$ might also be formed from the anisotropic growth of $Au_{24}(SR)_{20}$. In the synthesis by the Wu group, $Au_{42}(SR)_{32}$ nanocluster was obtained by thermally induced ligand-exchange reaction from $Au_{28}(SPh^tBu)_{20}$, and then purified by thin layer chromatography,[224] indicating that the anisotropic growth occurs simultaneously with *fcc*-to-*hcp* structural transformation.

Among the bimetallic NCs, $Au_{10}Ag_2(C{\equiv}CR)_3(dppy)_6$ (C≡CR = 2-pyridylethynyl, dppy = 2-pyridyldiphenylphosphine) has a trigonal bipyramidal $Au_{10}Ag_2$ core with Ag atoms at the two ends. The dual emission of the NC in solution includes i) the visible emission originating from metal-to-ligand charge transfer from Ag atoms to phosphine ligands and ii) the intense NIR emission which is associated with the participation of 2-pyridylethynyl in the frontier orbitals of the NC.[225] The $Pt_1Ag_{26}(SR)_{18}(PPh_3)_6$ (SR = $SPh(CH_3)_2$) NC has an I_h $Pt@Ag_{12}$ kernel with two Ag atoms at both ends. With the $Ag_{12}(SR)_{18}(PPh_3)_6$ shell wrapping on the surface, the bimetallic NC shows an overall rod shape. Compared to $Pt_1Ag_{24}(SR)_{18}$ with a $Pt@Ag_{12}$ kernel, the optical absorption spectrum of $Pt_1Ag_{26}(SR)_{18}$ is almost the same, but their electrochemical gaps are quite different (1.48 V vs. 1.89 V) due to the charge influence.[226] When replacing the central Pt with Au, the authors co-crystallized $[Au_1Ag_{26}(SR')_{18}(PPh_3)_6]^+$ and $[Au_1Ag_{24}(SR')_{18}]^-$ (SR' = $SPhC_2H_5$) into alternating stacking array along the [001] direction via weak C–H···π and π···π interactions and strong electrostatic interactions.[227]

Additionally, Sun et al. prepared quite many polyoxometalate-templated Ag NCs under solvothermal conditions, and some of the NCs possess rod-shaped structures. Selected works include Ag_{72} (a long Ag shell wrapping two linearly aligned $[EuW_{10}O_{36}]^{9-}$ anions);[228] Ag_{76} (two $Mo_6O_{22}^{8-}$ templates encaged in an Ag_{72} shell);[229] Ag_{80} (the inside Ag_{10} kernel is locked by a pair of $Mo_7O_{26}^{10-}$ anions and further encapsulated by an outer Ag_{70} shell);[230] and Ag_{90} (the dumbbell-shaped Ag_{90} cage covers two smaller SO_4^{2-} and two larger $W_5O_{19}^{8-}$ anions inside).[231] Compared to the linear Au coordination to two S atoms, a complete cage usually forms due to higher Ag-S coordination,[55] which is more flexible to accommodate the inner kernel shape. Note that these Ag^I NCs have no free valent electron as we discussed above for Au NCs.

Oblate nanoclusters

Heteroleptic $Au_{19}(C{\equiv}CPh)_9(dppa)_3$ (dppa = *N,N*-bis-(diphenyl-phosphino)amine) has an I_h Au_{13} kernel, and three V-shaped $Au_2(C{\equiv}CPh)_3$ motifs along the C_3 axis.[232] The alkynyl ligands are anchored on surface Au atoms via both σ and π bondings, which is different from the bonding mode of thiolate on Au. The NC shows two major absorption peaks at 1.25 and 2.25 eV, and orbital analysis indicates that the PhC≡C− groups actively participate in the frontier orbitals of the whole NC (Figure 8A). Although not mentioned in the original work, we here point out that the metal part of the NC resembles a tiny triangular disk despite that no (100) facet is found on the surface. Another alkynyl-protected $Au_{22}(C{\equiv}CR)_{18}$ NC (R = ^{t}Bu) also has a triangular shape in which a flattened cuboctahedral Au_{13} kernel is surrounded by three $Au_3(C{\equiv}CR)_4$ motifs.[233] The $Au_{22}(C{\equiv}CR)_{18}$ NC required a relatively weak reduction environment in the synthesis. Although the QY of the NC solution (in CH_2Cl_2) was only 0.4%, the solid-state emission yield of $Au_{22}(C{\equiv}CR)_{18}$ increased to 15% with a predominant lifetime of 1.37 μs.[234] The same Au_{22} NC could also be prepared using triethylamine as a mild reductant, and different C≡CR', including 3-ethynylthiophene (ETP-H), phenylacetylene (PA-H), 3-ethynyltoluene (ET-H), and 3-ethynylanisole (EA-H) were adopted. The PL QY was found to be dependent on the R group, and the highest QY = 4.6% (solution) was obtained when R = Ph (Figure 8C).[131]

Not only the rod-shaped structure can be achieved by connecting three I_h units via vertex sharing,[188] a cyclic structure (i.e., an oblate shape) is also realized in bimetallic $Pt_3Ag_{33}(PPh_3)_{12}Cl_8$ (Figure 8D, left) and trimetallic $Pt_3Au_{12}Ag_{21}(PPh_3)_{12}Cl_8$ NCs with three Pt atoms doped at the centers of three I_h M_{13} (M = Ag/Au) units. Since the cyclic

structure is composed of three I_h units, the whole shape can be regarded as a truncated triangular disk. A clear red-shift of the lowest energy peak was observed from 428 nm for mono-I_h $Pt_1Ag_{12}(dppm)_5(SR)_2$ (dppm = $Ph_2PCH_2PPh_2$, SR = $SPh(CH_3)_2$) to 557 nm for bi-I_h $Pt_2Ag_{23}(PPh_3)_{10}Cl_7$, then to 750 nm for cyclic tri-I_h $Pt_3Ag_{33}(PPh_3)_{12}Cl_8$ (Figure 8D, right).[235]

Zheng et. al reported that $Au_9Ag_{36}(SR)_{27}(PPh_3)_6$ (SR = $SPhCl_2$) has an Au_9 kernel encaged in a trigonal prismatic $Ag_{36}(SR)_{27}(PPh_3)_6$ shell.[236] This bimetallic NC can be viewed to have two dented (111) facets and three distorted (100) facets of *fcc* arrangement (Figure 8E). The same group also revealed an $Ag_{78}(SR)_{42}(dppp)_6$ NC (SR = $SPhCF_3$, dppp = $Ph_2P(CH_2)_3PPh_2$) with a triangular prismatic structure conformed to ideal D_3 symmetry (Figure 8F, left). When replacing the achiral dppp with chiral diphosphine, i.e., (2s,4s) or (2r,4r)-2,4-bis(diphenylphosphino) pentane, the flexible C–C–C of diphoshpine restricts the relative orientation of the four Ag-thiolate-phosphine moieties at the three side edge, resulting in enantioselectivity of the metal core (*R*- and *S*-Ag_{78}), with the maximum anisotropy factor up to 2×10^{-3} at 678 nm (Figure 8F, right).[237]

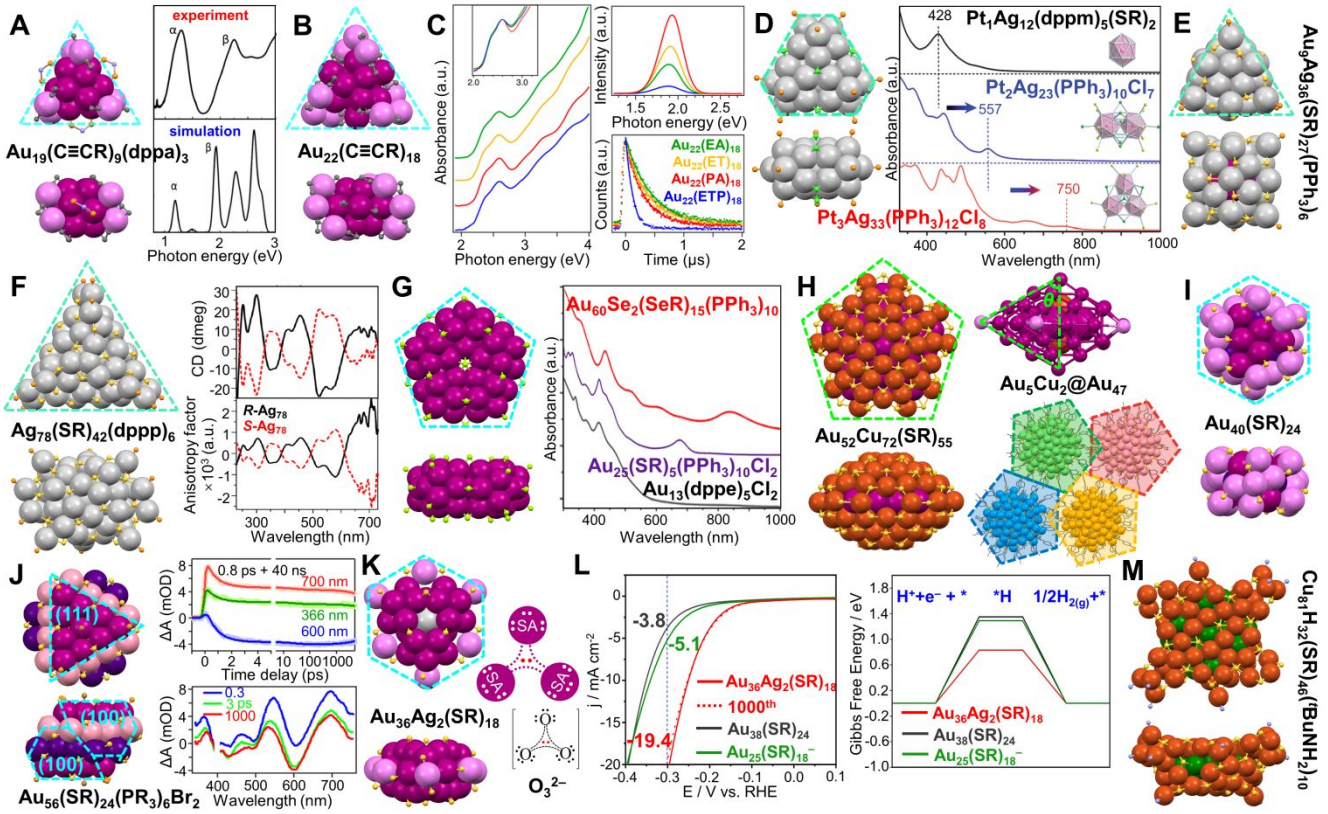

Figure 8. (A) Top and side views of $Au_{19}(C{\equiv}CR)_9(dppa)_3$, and its experimental and simulated optical absorption spectra. Reproduced with permission.[232] Copyright 2014, American Chemical Society. (B) Top and side views of $Au_{22}(C{\equiv}CR)_{18}$. (C) UV–vis spectra, PL spectra and lifetimes of $Au_{22}(C{\equiv}CR')_{18}$ with different ligands. Reproduced with permission.[131] Copyright 2019, American Chemical Society. (D) Top and side views of $Pt_3Ag_{33}(PPh_3)_{12}Cl_8$, and UV-vis spectra of $Pt_1Ag_{12}(dppm)_5(SR)_2$, $Pt_2Ag_{23}(PPh_3)_{10}Cl_7$, and $Pt_3Ag_{33}(PPh_3)_{12}Cl_8$. Reproduced with permission.[235] Copyright 2018, The Royal Society of Chemistry. (E) Top and side views of $Au_9Ag_{36}(SR)_{27}(PPh_3)_6$. (F) Top and side views of $Ag_{78}(SR)_{42}(dppp)_6$, and the CD spectra and corresponding anisotropy factors of *R*- and *S*-Ag_{78} enantiomers. Reproduced with permission.[237] Copyright 2017, American Chemical Society. (G) Top and side views of $Au_{60}Se_2(SeR)_{10}(PPh_3)_{15}$, and its UV-Vis spectrum compared to $Au_{25}(SR)_5(PPh_3)_{10}Cl_2$ and $Au_{13}(dppe)_5Cl_2$. Reproduced with permission.[238] Copyright 2015, Wiley-VCH GmbH. (H) Top and side views of $Au_{52}Cu_{72}(SR)_{55}$, its $Au_5Cu_2@Au_{47}$ decahedral kernel, and the interactions among four nearest pentagonal NCs. Reproduced with permission.[239] Copyright 2020, The author(s). (I) Top and side views of $Au_{40}(SR)_{24}$. (J) Top and side views of $Au_{56}(SR)_{24}(PR_3)_6Br_2$, the kinetic traces of transient absorption and corresponding fits at selected wavelengths, and spectra at selected time-delays. Reproduced with permission.[133] Copyright 2022, The author(s). (K) Top and side views of $Au_{36}Ag_2(SR)_{18}$, and the Lewis structure of the $[Au_{30}Ag_2]^{12+}$ kernel compared to O_3^{2-}, SA = superatom. (L) HER voltammograms of $Au_{36}Ag_2(SR)_{18}$, $Au_{38}(SR)_{24}$ and $Au_{25}(SR)_{18}^-$ catalysts, and the calculated Gibbs free energy of $H_2(g)$ formation on the catalysts. Reproduced with permission.[132] Copyright 2021, American Chemical Society. (M) Top and side views of $Cu_{81}H_{32}(SR)_{46}(^tBuNH_2)_{10}$. Color codes: magenta/violet/purple/pink = Au, light grey = Ag, orange/green = Cu, yellow = S, light orange = P, light green = Se, light purple = N. R groups are omitted or simplified for clarity.

Five I_h Au_{13} building blocks can even form a closed ring by vertex sharing in the $Au_{60}Se_2(SePh)_{15}(PPh_3)_{10}$ structure, which shows a pentagonal oblate shape. The two neighboring Au_{13} units are connected by selenolate linkages, and two Se atoms are capped at the top/bottom centers of the NC. The Au_{60} NC not only maintains the optical property of the Au_{13} unit, the interactions between neighboring Au_{13} units also lead to further red-shift of the low-energy absorption peak to 835 nm compared to the 670 nm peak of bi-I_h $Au_{25}(SR)_5(PPh_3)_{10}$ (Figure 8G).[238]

Oblate decahedral NCs have been reported when the kernel diameter reaches 2 nm. The thiolate (SR = SPh^tBu)-stabilized NC containing 374 Ag atoms was reported to become metallic with the emergence of surface plasmon resonance.[240] From the structural perspective, both Ag_{136} and Ag_{374} NCs are regarded as miniatures of five-fold twinned NPs. Ag_{136} has a

pentagonal bipyramidal Ag_{54} kernel with ten (111) facets, whereas Ag_{374} has an elongated pentagonal bipyramidal Ag_{207} kernel with five (100) faces at the five sides and five (111) facets at each end.[240] A decahedral Ag_{51} kernel with D_{5h} symmetry was also found in $Ag_{146}(SR')_{80}Br_2$ (SR' = $SPhCH(CH_3)_2$) with an overall pentagonal oblate shape.[241] Interestingly, the $Ag_{146}(SR')_{80}Br_2$ NC shows an optical bandgap and power-independent electron dynamics, indicating its molecular-like nature, as opposed to the plasmonic Ag_{136} NC with a smaller size. The bimetallic $Au_{130-x}Ag_x(SR)_{55}$ (avg. x = 98) also has a decahedral M_{54} kernel (M = Au/Ag) inside the Ag-SR shell. In the M_{54} kernel, all $Au_{\sim 32}$ atoms are localized in the truncated M_{49} Marks decahedron, whereas the five corners of the regular M_{54} decahedron are all Ag.[242] An interesting question is why homogold NCs of similar size can only have truncated Au_{49} kernel,[20,85] while Ag or Au/Ag alloy NCs show M_{54} full decahedrons inside the NCs. The case of $Au_{52}Cu_{72}(SR'')_{55}$ (SR'' = $SPhCH_3$) gives insights into the Marks decahedron truncation mechanism (Figure 8H). When comparing the $Au_5Cu_2@Au_{47}$ kernel (Figure 8H, top right) in the Au-Cu bimetallic NC and the $Au_7@Au_{42}$ kernel in $Au_{102}(SR)_{44}$ or $Au_{103}S_2(SR)_{41}$, it was found that the axial Au–Cu–Cu–Au length is contracted by 7% due to Cu doping, and the angle (θ) also expends, giving enough space for an Au atom to fit in (total five corners), completing a decahedral M_{54} core. The same phenomenon was also observed in Ag or Ag-Au bimetallic NCs, so that M_{54} full decahedrons are formed. Moreover, the $Cu_{70}(SR'')_{55}$ exterior cage of $Au_{52}Cu_{72}(SR'')_{55}$ resembles 3D Penrose tiling, and interparticle interactions in the supercrystal give rise to a "quadruple-gear-like" interlocking pattern (Figure 8H, bottom right).[239]

Tetrahedral Au_4 units coil up into a Kekulé-like ring along two vertex-sharing Au_4 units to constitute the *fcc* kernel in $Au_{40}(SR)_{24}$ (SR = $SPhCH_3$). Since the surface motifs are distributed along the C_3 axis, the whole NC demonstrates a hexagonal oblate structure.[87] In the seed-sized $Au_{56}(SR')_{24}(PR_3)_6Br_2$ (SR' = SPh^tBu, R = $PhCF_3$, PhCl, or PhF) nanoprism, the side Au{100} facets are covered by bridging thiolates, whereas the top or bottom {111} facet is capped by phosphine ligands at three corners and Br^- at the center (Figure 8I, left).[133] The bromide is key to effectively stabilize the Au{111} to fulfill a complete *fcc* core, while the halide-free gold precursor results in $Au_{55}(SR'')_{24}(PPh_3)_6$ (SR'' = $SPhCH_3$) with one missing gold on one of the two (111) facets.[243] Moreover, the femtosecond transient absorption spectrum of Au_{56} (Figure 8J, right) is similar to that of larger-sized gold NCs (n > 100), which is ascribed to the completeness of the prismatic *fcc* core.[133]

Beyond the Au_3 face-fusion of two I_h Au_{13} units to form the dimeric kernel of homogold and I_h-center-doped $Au_{38}(SR)_{24}$ NCs (see Figure 3A/C/D/G/H), the Jin group recently reported a $Au_{36}Ag_2(SR)_{18}$ (SR = SC_5H_{10}) NC in which three I_h units face-fused together in a cyclic way.[132] The series of NCs, i.e., mono-I_h $Au_{25}(SR')_{18}^-$, di-I_h $Au_{38}(SR')_{24}$ (SR' = SC_2H_4Ph) and tri-I_h $Au_{36}Ag_2(SR)_{18}$ (Figure 8K) is achieved with electron number increasing from $8e^-$ to $14e^-$ to $20e^-$, in contrast to the vertex-sharing I_h NC series with $8e^-$ to $16e^-$ to $24e^-$ electron configurations (Figure 8D). The two Ag atoms at the centers of the NC are found to be critical in achieving the trimeric face-fused structure, since the I_h central Au would take more electron density than the shell atoms[244] and the much less electronegative Ag atoms (χ_{Ag} = 1.93 vs χ_{Au} = 2.54) would be preferred at the two positions that are shared by all three I_h units. Since the $[Au_{30}Ag_2]^{12+}$ kernel can be viewed as a union of three face-fused superatoms, Cheng et al. performed chemical bonding analysis suggesting a three-superatom-center two-electron bond for the octet rule of each superatom, which mimics the bonding framework of the D_{3h} O_3^{2-} molecular anion (Figure 8K, right).[245] Moreover, the new series of NCs was used in a comparative study in hydrogen evolution reaction (HER). The tri-I_h NC exhibited high catalytic activity for HER due to its low ligand-to-metal ratio, low-coordinated Au atoms and unfilled superatomic orbitals, providing a new strategy for constructing highly active catalysts from HER-inert metals via atomically precise nanochemistry. The current density of $Au_{36}Ag_2(SR)_{18}$ at −0.3 V vs RHE was 3.8 and 5.1 times that of $Au_{25}(SR')_{18}^-$ and $Au_{38}(SR')_{24}$, respectively. DFT calculations also revealed lower hydrogen binding energy and higher electron affinity of $Au_{36}Ag_2(SR)_{18}$ (Figure 8L).[132]

Bakr et al. reported a $Cu_{81}H_{32}(SPh)_{46}(^tBuNH_2)_{10}$ NC with an unprecedented planar Cu_{17} kernel inside a hemispherical shell comprised of a curved surface layer and a planar surface layer (Figure 8M). This copper NC was synthesized with a mild reducing agent (borane tert-butylamine complex).[246] However, this NC does not have any valence electron.

Challenges and perspectives

The optical and chemical properties of NPs are strongly dependent on the particle size and shape. As the size of NPs shrinks to the ultrasmall regime (<3 nm in diameter), distinct optical properties with successive multiple absorption bands apprear because these ultrasmall NPs start to show quantized or molecular states.

One of the challenges is to design anisotropic NCs of atomic precision in hope that their optical properties can be tailored via anistropic growth. Indeed, as NCs grow from isotropic cubic or spherical structures to the rod shapes, one can see that the lowest-energy absorption band red-shifts to longer wavelengths (from visible to NIR region) no matter the kernel is icosahedral, *fcc*, or *hcp*. Note that only NCs with free valence electrons show tunable absorption bands, not metal complexes. The NIR absorption of atomically precise NCs shows great importance due to the potential applications including photothermal conversion and NIR emmision which are very useful in medical therapy and bioimaging, especially the NCs smaller than the 5.5 nm are below the renal clearance limit and thus can undergo rapid excretion by kidney.[247–249] But before we can effectively apply these atomically precise anisotropic NCs to real applications, some challenges remain.

The first challenge pertains to the methodology for the synthesis of anisotropic NCs at ultrasmall sizes is still not clear. However, some clues for future work are provided herein. Dimeric homogold and Pt/Pd doped $Au_{38}(SR)_{24}$ can be prepared by either direct reduction and separation,[75] or the recently developed method of fusion-mediated synthesis in which monomeric units are used in the precursor.[158] Both rod-shaped $Au_{25}(SR)_5(PPh_3)_{10}Cl_2$ and $Au_{37}(SR)_{10}(PPh_3)_{10}Cl_2$ NCs are synthesized by reducing $Au^I(PPh_3)Cl$ with $NaBH_4$ to cluster-

sized seeds, which further react with excess thiol upon moderate heating.[187,188] We suppose that in order to successfully produce rod-shaped NCs, seed NCs and additional metal salts should be involved together. The idea comes from the well-develped seed-mediated growth approach, in which the ratio of metallic spherical seeds to metal salt is controled in the reduction reaction to tune the aspect ratio of nanorods and nanowires.[250] Moreover, for rod-shaped Au NCs with *fcc* or *hcp* kernels, slow reduction is required to introduce anisotropic growth. Ultrathin Au nanorods with a constant diameter of ~2 nm (within the NC size regime) and tunable length (5–20 nm) were obtained by slow reducing Au^{I} in the presence of oleylamine, then ligand exchanging with thiolates. The ultrathin Au-SR nanorods show an intense band in the NIR and are not plamonic.[251] The phenomenon is later proved in the resolved $Au_{42}(SR)_{32}$ nanorods of atomic precision.[127] We expect that even longer close-packed kernels can be achieved by delicate kinetic control, however, the crystal growth of NCs with larger aspect ratios would be very challenging. In such case, high-angle annular dark field scanning TEM with ultra-low dose would be necessary to characterize the shape of the NCs.[252]

No matter how exciting the atomcially precise structure is, it is required to convert the organic soluble NCs into aqua phase for broader biological applications. In the case of rod-shaped $Au_{25-x}Ag_x(SR)_5(PPh_3)_{10}Cl_2$ (x = 1–13), the organic soluble thiolates are replaced by SC_2H_4OH so that the NCs can be used in fluorescence confocal imaging for living cancer cells.[179] $Au_{22}(SG)_{18}$ (SG = glutathione) NC can be used as biocompatible light absorber to overcome the slow kinetics of electron transfer, enabling photosynthesis of acetic acid from CO_2 when translocating into non-photosynthetic bacteria.[253] The Zhang group investigated the peptide ligands stablized Au_{25} NCs with NIR-II emission (1100–1350 nm). The bright luminescence enhanced by Cu or Zn doping could penetrate deeper into the tissue, and be applied in in vivo brain vessel imaging and tumor metastasis.[254] So far, very few biocompatable Au NCs of atomic precision have been synthesized using water-soluble ligands since it is very difficult for crystallization.[18,255,256] Therefore, looking for an effective way to transfer the organo-soluble NCs into aqua solution is highly desirable in future work.

The second challenge is to design NCs with regioselective surface functionalization. Anisotropic NPs are usually associated with distinctive self-assembly behavior,[257,258] making them quite attractive in fundamental research and various applications. In the NC regime, we have indeed observed the outstanding self-assemblies achieved by heterodimeric $Au_{29}(SR)_{19}$ NCs.[38] But many of the properties of this NC have not been fully understood, e.g., its much longer excited-state lifetime compared to that of the homodimeric counterpart, and its NIR emission, either. When coupling a pair of nonequivalent NPs to form a heterodimer, the out-of-phase plasmon mode is no longer silent, whereas the in-phase mode is only allowed for homodimers.[259] Thus, more experimental and theoretical works are needed on heterodimeric NCs to reveal the mechnisms in a more profound way. Moreover, noble metal (e.g., Ag) NPs can combine with magnetic (e.g., Fe_3O_4) NPs to form a bifunctional heterodimer for both fluorescnence imaging and magnetic manipulation.[260] It has been shown that a single $(SR)_3CdBr$ motif can be attached to the Au NC in atomic precision,[122] which can be regarded as a simplified heterodimeric combination. It is worth trying to attach heteroatoms, e.g., Zn, Ni, Rh, on the surface of group-10 metal NCs to achieve a regioselective surface with specific functionalization.

The third challenge is how to grow oblate NCs into large sizes. The anistropy of triangular metal nanoprisms show strong quadrupole plasmon excitation.[261–263] Introducing iodide ion leads to triangular Au nanoprisms,[264] and gold nanoprism growth could be controlled by slow reduction of Au ions onto the surface of seeding nanoprisms with the quadrupole plasmon resonance λ_{max} shifting with the nanoprism edge length.[265] Since the longitudinal transition has been confirmed in atomically precise NCs of rod-shape, we expect that quadrupole transitions might also be present in triangular oblate NCs. However, the much lower ratios of edge length to thickness in current oblate NCs limit such electronic transition. What we can conclude so far is that different ligands play different roles in the growth of anisotropic NCs of atomic precision, for example, halides always cap the two ends of the rod-shaped NCs or the Au(111) facets; phosphine ligands prefer to confine the corners of triangular, rectangular, or pentangular shapes; whereas thiolates tend to form a self-assembled monolayer on the Au {100} facets.[266] It is required that a triangular namnoprism of atomic precision can grow into a thinner sheet with larger planar surfaces, and a delicate control over the aspect ratio with different ligands is still necessary.

In conclusion, atomically precise metal NCs with anisotropic structures reported so far have been summarized, and their advantages over isotropic counterparts have been highlighted through comparison. While the synthesis of anisotropic NCs still remains a challenge, generally speaking, the presence of isotropic NC seeds in the precursor could be a way to prepare dimeric and rod-shaped NCs, and a very mild reducing environment is often required to prepare anisotropic nanostructures. With the longitudinal transition appeared in rod-shaped NCs and its tunability with the aspect ratio of the anisotropic structure, new physicochemical properties and applications have been observed and worth further studies in future research. The 2D or disk-shaped NCs also remain to be explored in terms of their unique properties and applications.

Conflicts of interest

There are no conflicts to declare.

Acknowledgements

R.J. acknowledges the financial support from the NSF (DMR-1808675).

Notes and references

1 C. Burda, X. Chen, R. Narayanan and M. A. El-Sayed, *Chem. Rev.*, 2005, **105**, 1025–1102.
2 M. Grzelczak, J. Pérez-Juste, P. Mulvaney and L. M. Liz-Marzán, *Chem. Soc. Rev.*, 2008, **37**, 1783–1791.
3 R. Jin, Y. Charles Cao, E. Hao, G. S. Métraux, G. C. Schatz and C. A. Mirkin, *Nature*, 2003, **425**, 487–490.
4 R. Narayanan and M. A. El-Sayed, *Nano Lett.*, 2004, **4**, 1343–1348.

5 C. J. Orendorff, T. K. Sau and C. J. Murphy, *Small*, 2006, **2**, 636–639.
6 J. N. Anker, W. P. Hall, O. Lyandres, N. C. Shah, J. Zhao and R. P. Van Duyne, *Nat. Mater.*, 2008, **7**, 442–453.
7 S. Cao, F. (Feng) Tao, Y. Tang, Y. Li and J. Yu, *Chem. Soc. Rev.*, 2016, **45**, 4747–4765.
8 J. Turkevich, P. C. Stevenson and J. Hillier, *Discuss. Faraday Soc.*, 1951, 55–75.
9 G. Ferns, *Nat. Phys. Sci.*, 1973, **241**, 20–22.
10 G. Schmid, *Chem. Rev.*, 1992, **92**, 1709–1727.
11 M.-C. Daniel and D. Astruc, *Chem. Rev.*, 2004, **104**, 293–346.
12 M. Giersig and P. Mulvaney, *Langmuir*, 1993, **9**, 3408–3413.
13 R. Elghanian, J. J. Storhoff, R. C. Mucic, R. L. Letsinger and C. A. Mirkin, *Science*, 1997, **277**, 1078–1081.
14 M. Brust, J. Fink, D. Bethell, D. J. Schiffrin and C. Kiely, *J. Chem. Soc., Chem. Commun.*, 1995, 1655–1656.
15 M. J. Hostetler, J. E. Wingate, C.-J. Zhong, J. E. Harris, R. W. Vachet, M. R. Clark, J. D. Londono, S. J. Green, J. J. Stokes, G. D. Wignall, G. L. Glish, M. D. Porter, N. D. Evans and R. W. Murray, *Langmuir*, 1998, **14**, 17–30.
16 R. L. Whetten, J. T. Khoury, M. M. Alvarez, S. Murthy, I. Vezmar, Z. L. Wang, P. W. Stephens, C. L. Cleveland, W. D. Luedtke and U. Landman, *Adv. Mater.*, 1996, **8**, 428–433.
17 S. Chen, R. S. Ingram, M. J. Hostetler, J. J. Pietron, R. W. Murray, T. G. Schaaff, J. T. Khoury, M. M. Alvarez and R. L. Whetten, *Science*, 1998, **280**, 2098–2101.
18 Y. Negishi, Y. Takasugi, S. Sato, H. Yao, K. Kimura and T. Tsukuda, *J. Am. Chem. Soc.*, 2004, **126**, 6518–6519.
19 Y. Negishi, K. Nobusada and T. Tsukuda, *J. Am. Chem. Soc.*, 2005, **127**, 5261–5270.
20 P. D. Jadzinsky, G. Calero, C. J. Ackerson, D. A. Bushnell and R. D. Kornberg, *Science*, 2007, **318**, 430–433.
21 M. Zhu, C. M. Aikens, F. J. Hollander, G. C. Schatz and R. Jin, *J. Am. Chem. Soc.*, 2008, **130**, 5883–5885.
22 M. W. Heaven, A. Dass, P. S. White, K. M. Holt and R. W. Murray, *J. Am. Chem. Soc.*, 2008, **130**, 3754–3755.
23 R. Jin, Y. Zhu and H. Qian, *Chem. Eur. J.*, 2011, **17**, 6584–6593.
24 R. Jin, C. Zeng, M. Zhou and Y. Chen, *Chem. Rev.*, 2016, **116**, 10346–10413.
25 I. Chakraborty and T. Pradeep, *Chem. Rev.*, 2017, **117**, 8208–8271.
26 M. Zhou, T. Higaki, G. Hu, M. Y. Sfeir, Y. Chen, D. Jiang and R. Jin, *Science*, 2019, **364**, 279–282.
27 Q. Yao, T. Chen, X. Yuan and J. Xie, *Acc. Chem. Res.*, 2018, **51**, 1338–1348.
28 N. Xia and Z. Wu, *Chem. Sci.*, 2021, **12**, 2368–2380.
29 T. Omoda, S. Takano and T. Tsukuda, *Small*, 2021, **17**, 2001439.
30 R. Jin, G. Li, S. Sharma, Y. Li and X. Du, *Chem. Rev.*, 2021, **121**, 567–648.
31 Y. Jiang, S. Alvarez and R. Hoffmann, *Inorg. Chem.*, 1985, **24**, 749–757.
32 Y. Li, M. Zhou and R. Jin, *Adv. Mater.*, 2021, 2006591.
33 R. Jin and T. Higaki, *Commun. Chem.*, 2021, **4**, 28.
34 H. Schmidbaur and A. Schier, *Chem. Soc. Rev.*, 2012, **41**, 370–412.
35 C. N. R. Rao, G. U. Kulkarni, P. J. Thomas and P. P. Edwards, *Chem. Soc. Rev.*, 2000, **29**, 27–35.
36 M. Walter, J. Akola, O. Lopez-Acevedo, P. D. Jadzinsky, G. Calero, C. J. Ackerson, R. L. Whetten, H. Grönbeck and H. Häkkinen, *Proc. Natl. Acad. Sci.*, 2008, **105**, 9157–9162.
37 T. Higaki, C. Liu, C. Zeng, R. Jin, Y. Chen, N. L. Rosi and R. Jin, *Angew. Chem. Int. Ed.*, 2016, **55**, 6694–6697.
38 Y. Li, M. Zhou, Y. Song, T. Higaki, H. Wang and R. Jin, *Nature*, 2021, **594**, 380–384.
39 C. E. Anson, A. Eichhöfer, I. Issac, D. Fenske, O. Fuhr, P. Sevillano, C. Persau, D. Stalke and J. Zhang, *Angew. Chem. Int. Ed.*, 2008, **47**, 1326–1331.
40 M.-L. Fu, I. Issac, D. Fenske and O. Fuhr, *Angew. Chem. Int. Ed.*, 2010, **49**, 6899–6903.
41 S. C. Riha, B. A. Parkinson and A. L. Prieto, *J. Am. Chem. Soc.*, 2011, **133**, 15272–15275.
42 P. K. Santra and P. V. Kamat, *J. Am. Chem. Soc.*, 2013, **135**, 877–885.
43 M. Zhou, T. Higaki, Y. Li, C. Zeng, Q. Li, M. Y. Sfeir and R. Jin, *J. Am. Chem. Soc.*, 2019, **141**, 19754–19764.
44 T. Higaki, M. Zhou, K. J. Lambright, K. Kirschbaum, M. Y. Sfeir and R. Jin, *J. Am. Chem. Soc.*, 2018, **140**, 5691–5695.
45 B. Yoon, W. D. Luedtke, R. N. Barnett, J. Gao, A. Desireddy, B. E. Conn, T. P. Bigioni and U. Landman, *Nat. Mater.*, 2014, **13**, 807–811.
46 C. Zeng, Y. Chen, K. Kirschbaum, K. J. Lambright and R. Jin, *Science*, 2016, **354**, 1580–1584.
47 J. Yan, S. Malola, C. Hu, J. Peng, B. Dittrich, B. K. Teo, H. Häkkinen, L. Zheng and N. Zheng, *Nat. Commun.*, 2018, 9:3357.
48 Y. Li and R. Jin, *J. Am. Chem. Soc.*, 2020, **142**, 13627–13644.
49 G. Li and R. Jin, *Acc. Chem. Res.*, 2013, **46**, 1749–1758.
50 M. M. Montemore, M. A. van Spronsen, R. J. Madix and C. M. Friend, *Chem. Rev.*, 2018, **118**, 2816–2862.
51 T. Higaki, Y. Li, S. Zhao, Q. Li, S. Li, X.-S. Du, S. Yang, J. Chai and R. Jin, *Angew. Chem. Int. Ed.*, 2019, **58**, 8291–8302.
52 Y. Du, H. Sheng, D. Astruc and M. Zhu, *Chem. Rev.*, 2020, **120**, 526–622.
53 X.-K. Wan, S.-F. Yuan, Z.-W. Lin and Q.-M. Wang, *Angew. Chem. Int. Ed.*, 2014, **53**, 2923–2926.
54 R. L. Whetten, H.-C. Weissker, J. J. Pelayo, S. M. Mullins, X. López-Lozano and I. L. Garzón, *Acc. Chem. Res.*, 2019, **52**, 34–43.
55 Y. Li, T. Higaki, X. Du and R. Jin, *Adv. Mater.*, 2020, 1905488.
56 S. Chen, W. Du, C. Qin, D. Liu, L. Tang, Y. Liu, S. Wang and M. Zhu, *Angew. Chem. Int. Ed.*, 2020, **59**, 7542–7547.
57 J. Pérez-Juste, I. Pastoriza-Santos, L. M. Liz-Marzán and P. Mulvaney, *Coord. Chem. Rev.*, 2005, **249**, 1870–1901.
58 A. R. Tao, S. Habas and P. Yang, *Small*, 2008, **4**, 310–325.
59 M. Rycenga, C. M. Cobley, J. Zeng, W. Li, C. H. Moran, Q. Zhang, D. Qin and Y. Xia, *Chem. Rev.*, 2011, **111**, 3669–3712.
60 M. L. Personick and C. A. Mirkin, *J. Am. Chem. Soc.* 2013, **135**, 18238–18247.
61 E. C. Dreaden, A. M. Alkilany, X. Huang, C. J. Murphy and M. A. El-Sayed, *Chem. Soc. Rev.*, 2012, **41**, 2740–2779.
62 H. Duan, D. Wang and Y. Li, *Chem. Soc. Rev.*, 2015, **44**, 5778–5792.
63 X. M. Lin, H. M. Jaeger, C. M. Sorensen and K. J. Klabunde, *J. Phys. Chem. B*, 2001, **105**, 3353–3357.
64 J. Th. G. Overbeek, *Adv. Colloid Interface Sci.*, 1982, **15**, 251–277.
65 K. R. Brown, D. G. Walter and M. J. Natan, *Chem. Mater.*, 2000, **12**, 306–313.
66 N. R. Jana, L. Gearheart and C. J. Murphy, *Langmuir*, 2001, **17**, 6782–6786.
67 Y. Zheng, X. Zhong, Z. Li and Y. Xia, *Part. Part. Syst. Charact.*, 2014, **31**, 266–273.
68 Z. Wu, J. Suhan and R. Jin, *J. Mater. Chem.*, 2009, **19**, 622–626.
69 W. Zhang, J. Kong, Y. Li, Z. Kuang, H. Wang and M. Zhou, *Chem. Sci.*, 2022, **13**, 8124–8130.
70 H. Qian, Y. Zhu and R. Jin, *Proc. Natl. Acad. Sci.*, 2012, **109**, 696–700.
71 T. Higaki, M. Zhou, G. He, S. D. House, M. Y. Sfeir, J. C. Yang and R. Jin, *Proc. Natl. Acad. Sci.*, 2019, **116**, 13215–13220.
72 R. Jin, *Nanoscale*, 2010, **2**, 343–362.
73 H. Qian, M. Zhu, Z. Wu and R. Jin, *Acc. Chem. Res.*, 2012, **45**, 1470–1479.
74 R. Jin, H. Qian, Z. Wu, Y. Zhu, M. Zhu, A. Mohanty and N. Garg, *J. Phys. Chem. Lett.*, 2010, **1**, 2903–2910.
75 H. Qian, Y. Zhu and R. Jin, *ACS NANO*, 2009, **3**, 3795–3803.
76 H. Qian, W. T. Eckenhoff, Y. Zhu, T. Pintauer and R. Jin, *J. Am. Chem. Soc.*, 2010, **132**, 8280–8281.
77 H. Qian and R. Jin, *Nano Lett.*, 2009, **9**, 4083–4087.
78 N. Yan, N. Xia, L. Liao, M. Zhu, F. Jin, R. Jin and Z. Wu, *Sci Adv*, 2018, 4:eaat7259.
79 C. Zeng, H. Qian, T. Li, G. Li, N. L. Rosi, B. Yoon, R. N. Barnett, R. L. Whetten, U. Landman and R. Jin, *Angew. Chem. Int. Ed.*, 2012, **51**, 13114–13118.
80 C. Zeng, T. Li, A. Das, N. L. Rosi and R. Jin, *J. Am. Chem. Soc.*, 2013, **135**, 10011–10013.
81 C. Zeng, C. Liu, Y. Chen, N. L. Rosi and R. Jin, *J. Am. Chem. Soc.*, 2014, **136**, 11922–11925.
82 A. Das, T. Li, G. Li, K. Nobusada, C. Zeng, N. L. Rosi and R. Jin, *Nanoscale*, 2014, **6**, 6458–6462.
83 C. Zeng, Y. Chen, K. Kirschbaum, K. Appavoo, M. Y. Sfeir and R. Jin, *Sci. Adv.*, 2015, 1:e1500045.
84 H. Dong, L. Liao and Z. Wu, *J. Phys. Chem. Lett.*, 2017, **8**, 5338–5343.
85 T. Higaki, C. Liu, M. Zhou, T.-Y. Luo, N. L. Rosi and R. Jin, *J. Am. Chem. Soc.*, 2017, **139**, 9994–10001.

86 Y. Chen, C. Zeng, D. R. Kauffman and R. Jin, *Nano Letters*, 2015, **15**, 3603–3609.
87 C. Zeng, Y. Chen, C. Liu, K. Nobusada, N. L. Rosi and R. Jin, *Sci. Adv.*, 2015, 1:e1500425.
88 Y. Chen, C. Zeng, C. Liu, K. Kirschbaum, C. Gayathri, R. R. Gil, N. L. Rosi and R. Jin, *J. Am. Chem. Soc.*, 2015, **137**, 10076–10079.
89 Z. Gan, N. Xia and Z. Wu, *Acc. Chem. Res.*, 2018, **51**, 2774–2783.
90 S. Wang, Q. Li, X. Kang and M. Zhu, *Acc. Chem. Res.*, 2018, **51**, 2784–2792.
91 S. Hossain, Y. Niihori, L. V. Nair, B. Kumar, W. Kurashige and Y. Negishi, *Acc. Chem. Res.*, 2018, **51**, 3114–3124.
92 A. Ghosh, O. F. Mohammed and O. M. Bakr, *Acc. Chem. Res.*, 2018, **51**, 3094–3103.
93 S. Eustis and M. A. El-Sayed, *Chem. Soc. Rev.*, 2006, **35**, 209–217.
94 J. E. Millstone, S. J. Hurst, G. S. Métraux, J. I. Cutler and C. A. Mirkin, *Small*, 2009, **5**, 646–664.
95 T. S. Ahmadi, Z. L. Wang, T. C. Green, A. Henglein and M. A. El-Sayed, *Science*, 1996, **272**, 1924–1925.
96 Y. Sun and Y. Xia, *Science*, 2002, **298**, 2176–2179.
97 M. R. Langille, M. L. Personick, J. Zhang and C. A. Mirkin, *J. Am. Chem. Soc.*, 2012, **134**, 14542–14554.
98 C. J. Murphy, A. M. Gole, S. E. Hunyadi and C. J. Orendorff, *Inorg. Chem.*, 2006, **45**, 7544–7554.
99 S. E. Lohse and C. J. Murphy, *Chem. Mater.*, 2013, **25**, 1250–1261.
100 A. Gole and C. J. Murphy, *Chem. Mater.*, 2004, **16**, 3633–3640.
101 F. Kim, J. H. Song and P. Yang, *J. Am. Chem. Soc.*, 2002, **124**, 14316–14317.
102 Y.-Y. Yu, S.-S. Chang, C.-L. Lee and C. R. C. Wang, *J. Phys. Chem. B*, 1997, **101**, 6661–6664.
103 C. Sönnichsen and A. P. Alivisatos, *Nano Lett.*, 2005, **5**, 301–304.
104 J. Becker, A. Trügler, A. Jakab, U. Hohenester and C. Sönnichsen, *Plasmonics*, 2010, **5**, 161–167.
105 L. Vigderman, B. P. Khanal and E. R. Zubarev, *Adv. Mater.*, 2012, **24**, 4811–4841.
106 Y. W. C. Cao, R. Jin and C. A. Mirkin, *Science*, 2002, **297**, 1536–1540.
107 H. Chen, L. Shao, Q. Li and J. Wang, *Chem. Soc. Rev.*, 2013, **42**, 2679–2724.
108 P. Zijlstra, P. M. R. Paulo and M. Orrit, *Nat. Nanotechnol.*, 2012, **7**, 379–382.
109 V. Amendola, R. Pilot, M. Frasconi, O. M. Maragò and M. A. Iatì, *J. Phys. Condens. Matter*, 2017, **29**, 203002.
110 M. Yu and J. Zheng, *ACS Nano*, 2015, **9**, 6655–6674.
111 L. Tong, Q. Wei, A. Wei and J.-X. Cheng, *Photochem. Photobiol.*, 2009, **85**, 21–32.
112 J. Chen, C. Glaus, R. Laforest, Q. Zhang, M. Yang, M. Gidding, M. J. Welch and Y. Xia, *Small*, 2010, **6**, 811–817.
113 S. M. Moghimi, A. C. Hunter and J. C. Murray, *Pharmacol. Rev.*, 2001, **53**, 283.
114 M. Ferrari, *Nat. Rev. Cancer*, 2005, **5**, 161–171.
115 N. L. Rosi and C. A. Mirkin, *Chem. Rev.*, 2005, **105**, 1547–1562.
116 X. Huang, P. K. Jain, I. H. El-Sayed and M. A. El-Sayed, *Nanomedicine*, 2007, **2**, 681–693.
117 A. Albanese, P. S. Tang and W. C. W. Chan, *Annu. Rev. Biomed. Eng.*, 2012, **14**, 1–16.
118 A. Desireddy, B. E. Conn, J. Guo, B. Yoon, R. N. Barnett, B. M. Monahan, K. Kirschbaum, W. P. Griffith, R. L. Whetten, U. Landman and T. P. Bigioni, *Nature*, 2013, **501**, 399–402.
119 Y. Wang, X.-K. Wan, L. Ren, H. Su, G. Li, S. Malola, S. Lin, Z. Tang, H. Häkkinen, B. K. Teo, Q.-M. Wang and N. Zheng, *J. Am. Chem. Soc.*, 2016, **138**, 3278–3281.
120 F. Hu, Z.-J. Guan, G. Yang, J.-Q. Wang, J.-J. Li, S.-F. Yuan, G.-J. Liang and Q.-M. Wang, *J. Am. Chem. Soc.*, 2021, **143**, 17059–17067.
121 I. Dolamic, S. Knoppe, A. Dass and T. Bürgi, *Nat. Commun.*, 2012, 3:798.
122 Y. Li, M. J. Cowan, M. Zhou, M. G. Taylor, H. Wang, Y. Song, G. Mpourmpakis and R. Jin, *ACS Nano*, 2020, **14**, 6599–6606.
123 Z. Wu, G. Hu, D. Jiang, D. R. Mullins, Q.-F. Zhang, L. F. Allard, L.-S. Wang and S. H. Overbury, *Nano Lett.*, 2016, **16**, 6560–6567.
124 V. K. Kulkarni, B. N. Khiarak, S. Takano, S. Malola, E. L. Albright, T. I. Levchenko, M. D. Aloisio, C.-T. Dinh, T. Tsukuda, H. Häkkinen and C. M. Crudden, *J. Am. Chem. Soc.*, 2022, **144**, 9000–9006.
125 L. Liao, C. Wang, S. Zhuang, N. Yan, Y. Zhao, Y. Yang, J. Li, H. Deng and Z. Wu, *Angew. Chem. Int. Ed.*, 2020, **59**, 731–734.
126 Z. Gan, Y. Lin, L. Luo, G. Han, W. Liu, Z. Liu, C. Yao, L. Weng, L. Liao, J. Chen, X. Liu, Y. Luo, C. Wang, S. Wei and Z. Wu, *Angew. Chem. Int. Ed.*, 2016, **55**, 11567–11571.
127 Y. Li, Y. Song, X. Zhang, T. Liu, T. Xu, H. Wang, D. Jiang and R. Jin, *J. Am. Chem. Soc.*, 2022, **144**, 12381–12389.
128 L. Luo, Z. Liu, X. Du and R. Jin, *J. Am. Chem. Soc.*, 2022, **144**, 19243–19247.
129 Y. Shichibu and K. Konishi, *Inorg. Chem.*, 2013, **52**, 6570–6575.
130 M. Zhou, R. Jin, M. Y. Sfeir, Y. Chen, Y. Song and R. Jin, *Proc. Natl. Acad. Sci.*, 2017, **114**, E4697–E4705.
131 S. Ito, S. Takano and T. Tsukuda, *J. Phys. Chem. Lett.*, 2019, **10**, 6892–6896.
132 Y. Li, S. Li, A. V. Nagarajan, Z. Liu, S. Nevins, Y. Song, G. Mpourmpakis and R. Jin, *J. Am. Chem. Soc.*, 2021, **143**, 11102–11108.
133 Y. Song, Y. Li, M. Zhou, H. Li, T. Xu, C. Zhou, F. Ke, D. Huo, Y. Wan, J. Jie, W. W. Xu, M. Zhu and R. Jin, *Nat. Commun.*, 2022, 13:1235.
134 G. Chen, Y. Wang, L. H. Tan, M. Yang, L. S. Tan, Y. Chen and H. Chen, *J. Am. Chem. Soc.*, 2009, **131**, 4218–4219.
135 K. L. Wustholz, A.-I. Henry, J. M. McMahon, R. G. Freeman, N. Valley, M. E. Piotti, M. J. Natan, G. C. Schatz and R. P. Van Duyne, *J. Am. Chem. Soc.*, 2010, **132**, 10903–10910.
136 X. Liu, G. Saranya, X. Huang, X. Cheng, R. Wang, M. Chen, C. Zhang, T. Li and Y. Zhu, *Angew. Chem. Int. Ed.*, 2020, **59**, 13941–13946.
137 X. Cai, W. Hu, S. Xu, D. Yang, M. Chen, M. Shu, R. Si, W. Ding and Y. Zhu, *J. Am. Chem. Soc.*, 2020, **142**, 4141–4153.
138 Z.-H. Gao, K. Wei, T. Wu, J. Dong, D. Jiang, S. Sun and L.-S. Wang, *J. Am. Chem. Soc.*, 2022, **144**, 5258–5262.
139 S.-F. Yuan, J.-J. Li, Z.-J. Guan, Z. Lei and Q.-M. Wang, *Chem. Commun.*, 2020, **56**, 7037–7040.
140 J. Xu, L. Xiong, X. Cai, S. Tang, A. Tang, X. Liu, Y. Pei and Y. Zhu, *Chem. Sci.*, 2022, **13**, 2778–2782.
141 A. Das, T. Li, K. Nobusada, Q. Zeng, N. L. Rosi and R. Jin, *J. Am. Chem. Soc.*, 2012, **134**, 20286–20289.
142 J. Chen, Q.-F. Zhang, T. A. Bonaccorso, P. G. Williard and L.-S. Wang, *J. Am. Chem. Soc.*, 2014, **2014**, 92–95.
143 J. Dong, Z.-H. Gao, Q.-F. Zhang and L.-S. Wang, *Angew. Chem. Int. Ed.*, 2021, **60**, 2424–2430.
144 S. Jin, X. Zou, L. Xiong, W. Du, S. Wang, Y. Pei and M. Zhu, *Angew. Chem. Int. Ed.*, 2018, **57**, 16768–16772.
145 O. Lopez-Acevedo, H. Tsunoyama, T. Tsukuda, H. Häkkinen and C. M. Aikens, *J. Am. Chem. Soc.*, 2010, **132**, 8210–8218.
146 L. Cheng, C. Ren, X. Zhang and J. Yang, *Nanoscale*, 2013, **5**, 1475–1478.
147 L. Cheng and J. Yang, *J. Chem. Phys.*, 2013, **138**, 141101.
148 Y. Li, R. Juarez-Mosqueda, Y. Song, Y. Zhang, J. Chai, G. Mpourmpakis and R. Jin, *Nanoscale*, 2020, **12**, 9423–9429.
149 M. S. Devadas, S. Bairu, H. Qian, E. Sinn, R. Jin and G. Ramakrishna, *J. Phys. Chem. Lett.*, 2011, **2**, 2752–2758.
150 C. Kumara and A. Dass, *Nanoscale*, 2012, **4**, 4084–4086.
151 C. Kumara, K. J. Gagnon and A. Dass, *J. Phys. Chem. Lett.*, 2015, **6**, 1223–1228.
152 J. Chai, Y. Lv, S. Yang, Y. Song, X. Zan, Q. Li, H. Yu, M. Wu and M. Zhu, *J. Phys. Chem. C*, 2017, **121**, 21665–21669.
153 Y. Negishi, K. Igarashi, K. Munakata, W. Ohgake and K. Nobusada, *Chem. Commun.*, 2012, **48**, 660–662.
154 M. Kim, Q. Tang, A. V. Narendra Kumar, K. Kwak, W. Choi, D. Jiang and D. Lee, *J. Phys. Chem. Lett.*, 2018, **9**, 982–989.
155 B. Zhang, S. Kaziz, H. Li, D. Wodka, S. Malola, O. Safonova, M. Nachtegaal, C. Mazet, I. Dolamic, J. Llorca, E. Kalenius, L. M. L. Daku, H. Häkkinen, T. Bürgi and N. Barrabés, *Nanoscale*, 2015, **7**, 17012–17019.
156 N. Barrabés, B. Zhang and T. Bürgi, *J. Am. Chem. Soc.*, 2014, **136**, 14361–14364.
157 E. Ito, S. Takano, T. Nakamura and T. Tsukuda, *Angew. Chem. Int. Ed.*, 2021, **60**, 645–649.
158 E. Ito, S. Ito, S. Takano, T. Nakamura and T. Tsukuda, *JACS Au*, 2022, **2**, 2627–2634.
159 X. Liu, E. Wang, M. Zhou, Y. Wan, Y. Zhang, H. Liu, Y. Zhao, J. Li, Y. Gao and Y. Zhu, *Angew. Chem. Int. Ed.*, 2022, **61**, e202207685.

160 S. Lee, M. S. Bootharaju, G. Deng, S. Malola, H. Häkkinen, N. Zheng and T. Hyeon, *J. Am. Chem. Soc.*, 2021, **143**, 12100–12107.
161 T. Dainese, S. Antonello, S. Bogialli, W. Fei, A. Venzo and F. Maran, *ACS NANO*, 2018, **12**, 7057–7066.
162 S. Tian, Y.-Z. Li, M.-B. Li, J. Yuan, J. Yang, Z. Wu and R. Jin, *Nat. Commun.*, 2015, 6:8667.
163 Z. Wang, R. Senanayake, C. M. Aikens, W.-M. Chen, C.-H. Tung and D. Sun, *Nanoscale*, 2016, **8**, 18905–18911.
164 K. Nunokawa, M. Ito, T. Sunahara, S. Onaka, T. Ozeki, H. Chiba, Y. Funahashi, H. Masuda, T. Yonezawa, H. Nishihara, M. Nakamoto and M. Yamamoto, *Dalton Trans.*, 2005, 2726–2730.
165 X.-K. Wan, Z.-W. Lin and Q.-M. Wang, *J. Am. Chem. Soc.*, 2012, **134**, 14750–14752.
166 Y. Li, M. G. Taylor, T.-Y. Luo, Y. Song, N. L. Rosi, G. Mpourmpakis and R. Jin, *J. Phys. Chem. Lett.*, 2020, **11**, 7307–7312.
167 L. Xiong, B. Peng, Z. Ma, P. Wang and Y. Pei, *Nanoscale*, 2017, **9**, 2895–2902.
168 Y. Chen, C. Liu, Q. Tang, C. Zeng, T. Higaki, A. Das, D. -e. Jiang, N. L. Rosi and R. Jin, *J. Am. Chem. Soc.*, 2016, **138**, 1482–1485.
169 W. Du, S. Deng, S. Chen, S. Jin, Y. Zhen, Y. Pei and M. Zhu, *J. Phys. Chem. Lett.*, 2021, **12**, 6654–6660.
170 X. Wei, H. Shen, C. Xu, H. Li, S. Jin, X. Kang and M. Zhu, *Inorg. Chem.*, 2021, **60**, 5931–5936.
171 Y. Song, S. Weng, H. Li, H. Yu and M. Zhu, *Inorg. Chem.*, 2019, **58**, 7136–7140.
172 Q. Li, K. J. Lambright, M. G. Taylor, K. Kirschbaum, T.-Y. Luo, J. Zhao, G. Mpourmpakis, S. Mokashi-Punekar, N. L. Rosi and R. Jin, *J. Am. Chem. Soc.*, 2017, **139**, 17779–17782.
173 S. Li, A. V. Nagarajan, D. R. Alfonso, M. Sun, D. R. Kauffman, G. Mpourmpakis and R. Jin, *Angew. Chem. Int. Ed.*, 2021, **60**, 6351–6356.
174 Y. Kamei, Y. Shichibu and K. Konishi, *Angew. Chem. Int. Ed.*, 2011, **50**, 7442–7445.
175 Y. Shichibu, Y. Kamei and K. Konishi, *Chem. Commun.*, 2012, **48**, 7559–7561.
176 N. Kobayashi, Y. Kamei, Y. Shichibu and K. Konishi, *J. Am. Chem. Soc.*, 2013, **135**, 16078–16081.
177 K. Konishi, M. Iwasaki and Y. Shichibu, *Acc. Chem. Res.*, 2018, **51**, 3125–3133.
178 Md. A. Bakar, M. Sugiuchi, M. Iwasaki, Y. Shichibu and K. Konishi, *Nat. Commun.*, 2017, 8:576.
179 S. Wang, X. Meng, A. Das, T. Li, Y. Song, T. Cao, X. Zhu, M. Zhu and R. Jin, *Angew. Chem. Int. Ed.*, 2014, **53**, 2376–2380.
180 H. Shen, G. Deng, S. Kaappa, T. Tan, Y.-Z. Han, S. Malola, S.-C. Lin, B. K. Teo, H. Häkkinen and N. Zheng, *Angew. Chem. Int. Ed.*, 2019, **58**, 17731–17735.
181 S.-F. Yuan, C.-Q. Xu, W.-D. Liu, J.-X. Zhang, J. Li and Q.-M. Wang, *J. Am. Chem. Soc.*, 2021, **143**, 12261–12267.
182 T.-H. Chiu, J.-H. Liao, F. Gam, I. Chantrenne, S. Kahlal, J.-Y. Saillard and C. W. Liu, *J. Am. Chem. Soc.*, 2019, **141**, 12957–12961.
183 B. K. Teo and H. Zhang, *Inorg. Chem.*, 1991, **30**, 3115–3116.
184 B. K. Teo, H. Zhang and X. Shi, *J. Am. Chem. Soc.*, 1990, **112**, 8552–8562.
185 B. K. Teo and H. Zhang, *Coord. Chem. Rev.*, 1995, **143**, 611–636.
186 Y. Shichibu, Y. Negishi, T. Tsukuda and T. Teranishi, *J. Am. Chem. Soc.*, 2005, **127**, 13464–13465.
187 Y. Shichibu, Y. Negishi, T. Watanabe, N. K. Chaki, H. Kawaguchi and T. Tsukuda, *J. Phys. Chem. C*, 2007, **111**, 7845–7847.
188 R. Jin, C. Liu, S. Zhao, A. Das, H. Xing, C. Gayathri, Y. Xing, N. L. Rosi, R. R. Gil and R. Jin, *ACS NANO*, 2015, **9**, 8530–8536.
189 Y. Shichibu and K. Konishi, *Small*, 2010, **6**, 1216–1220.
190 D. M. P. Mingos, *J. Chem. Soc., Chem. Commun.*, 1985, 1352–1354.
191 K. Nobusada and T. Iwasa, *J. Phys. Chem. C*, 2007, **111**, 14279–14282.
192 M. Y. Sfeir, H. Qian, K. Nobusada and R. Jin, *J. Phys. Chem. C*, 2011, **115**, 6200–6207.
193 S. Park and D. Lee, *Langmuir*, 2012, **28**, 7049–7054.
194 S. Chen, H. Ma, J. W. Padelford, W. Qinchen, W. Yu, S. Wang, M. Zhu and G. Wang, *J. Am. Chem. Soc.*, 2019, **141**, 9603–9609.
195 X. Kang, J. Xiang, Y. Lv, W. Du, H. Yu, S. Wang and M. Zhu, *Chem. Mater.*, 2017, **29**, 6856–6862.
196 L. V. Nair, S. Hossain, S. Takagi, Y. Imai, G. Hu, S. Wakayama, B. Kumar, W. Kurashige, D. Jiang and Y. Negishi, *Nanoscale*, **2018**, 18969–18979.
197 M. S. Bootharaju, S. M. Kozlov, Z. Cao, M. Harb, N. Maity, A. Shkurenko, M. R. Parida, M. N. Hedhili, M. Eddaoudi, O. F. Mohammed, O. M. Bakr, L. Cavallo and J.-M. Basset, *J. Am. Chem. Soc.*, 2017, **139**, 1053–1056.
198 S. Hossain, S. Miyajima, T. Iwasa, R. Kaneko, T. Sekine, A. Ikeda, T. Kawawaki, T. Taketsugu and Y. Negishi, *J. Chem. Phys.*, 2021, **155**, 024302.
199 F. Gam, C. W. Liu, S. Kahlal and J.-Y. Saillard, *Nanoscale*, 2020, **12**, 20308–20316.
200 S.-F. Yuan, Z.-J. Guan, W.-D. Liu and Q.-M. Wang, *Nat. Commun.*, 2019, 10:4032.
201 C. Zeng, Y. Chen, K. Iida, K. Nobusada, K. Kirschbaum, K. J. Lambright and R. Jin, *J. Am. Chem. Soc.*, 2016, **138**, 3950–3953.
202 W. W. Xu, X. Duan and X. C. Zeng, *J. Phys. Chem. Lett.*, 2020, **11**, 536–540.
203 S. Zhuang, L. Liao, Y. Zhao, J. Yuan, C. Yao, X. Liu, J. Li, H. Deng, J. Yang and Z. Wu, *Chem. Sci.*, 2018, **9**, 2437–2442.
204 S. Takano, S. Yamazoe, K. Koyasu and T. Tsukuda, *J. Am. Chem. Soc.*, 2015, **137**, 7027–7030.
205 W. W. Xu, Y. Li, Y. Gao and X.-C. Zeng, *Nanoscale*, 2016, **8**, 7396–7401.
206 Z. Ma, P. Wang, G. Zhou, J. Tang, H. Li and Y. Pei, *J. Phys. Chem. C*, 2016, **120**, 13739–13748.
207 S. Yang, J. Chai, Y. Song, X. Kang, H. Sheng, H. Chong and M. Zhu, *J. Am. Chem. Soc.*, 2015, **137**, 10033–10035.
208 H. Yang, J. Lei, B. Wu, Y. Wang, M. Zhou, A. Xia, L. Zheng and N. Zheng, *Chem. Commun.*, 2013, **49**, 300–302.
209 C. Liu, T. Li, H. Abroshan, Z. Li, C. Zhang, H. J. Kim, G. Li and R. Jin, *Nat. Commun.*, 2018, 9:744.
210 H. Yang, J. Yan, Y. Wang, H. Su, L. Gell, X. Zhao, C. Xu, B. K. Teo, H. Häkkinen and N. Zheng, *J. Am. Chem. Soc.*, 2017, **139**, 31–34.
211 M. J. Alhilaly, M. S. Bootharaju, C. P. Joshi, T. M. Besong, A.-H. Emwas, R. Juarez-Mosqueda, S. Kaappa, S. Malola, K. Adil, A. Shkurenko, H. Häkkinen, M. Eddaoudi and O. M. Bakr, *J. Am. Chem. Soc.*, 2016, **138**, 14727–14732.
212 C. Zeng, C. Liu, Y. Chen, N. L. Rosi and R. Jin, *J. Am. Chem. Soc.*, 2016, **138**, 8710–8713.
213 S. Zhuang, L. Liao, M.-B. Li, C. Yao, Y. Zhao, H. Dong, J. Li, H. Deng, L. Li and Z. Wu, *Nanoscale*, 2017, **9**, 14809–14813.
214 J.-Q. Wang, S. Shi, R.-L. He, S.-F. Yuan, G.-Y. Yang, G.-J. Liang and Q.-M. Wang, *J. Am. Chem. Soc.*, 2020, **142**, 18086–18092.
215 M. Zhu, H. Qian and R. Jin, *J. Phys. Chem. Lett.*, 2010, **1**, 1003–1007.
216 Y. Pei, R. Pal, C. Liu, Y. Gao, Z. Zhang and X. C. Zeng, *J. Am. Chem. Soc.*, 2012, **134**, 3015–3024.
217 Y. Song, S. Wang, J. Zhang, X. Kang, S. Chen, P. Li, H. Sheng and M. Zhu, *J. Am. Chem. Soc.*, 2014, **136**, 2963–2965.
218 A. Das, C. Liu, H. Y. Byun, K. Nobusada, S. Zhao, N. L. Rosi and R. Jin, *Angew. Chem. Int. Ed.*, 2015, **54**, 3140–3144.
219 S. Chen, S. Wang, J. Zhong, Y. Song, J. Zhang, H. Sheng, Y. Pei and M. Zhu, *Angew. Chem. Int. Ed.*, 2015, **54**, 3145–3149.
220 J. Xiang, P. Li, Y. Song, X. Liu, H. Chong, S. Jin, Y. Pei, X. Yuan and M. Zhu, *Nanoscale*, 2015, **7**, 18278–18283.
221 T. Higaki, C. Liu, C. Zeng, R. Jin, Y. Chen, N. L. Rosi and R. Jin, *Angew. Chem. Int. Ed.*, 2016, **55**, 6694–6697.
222 M. R. K. Ali, M. A. Rahman, Y. Wu, T. Han, X. Peng, M. A. Mackey, D. Wang, H. J. Shin, Z. G. Chen, H. Xiao, R. Wu, Y. Tang, D. M. Shin and M. A. El-Sayed, *Proc Natl Acad Sci USA*, 2017, **114**, E3110.
223 X. Jiang, B. Du, S. Tang, J.-T. Hsieh and J. Zheng, *Angew. Chem. Int. Ed.*, 2019, **58**, 5994–6000.
224 W. Fan, Y. Yang, Q. You, J. Li, H. Deng, N. Yan and Z. Wu, *J. Phys. Chem. C*, 2023, **127**, 816–823.
225 Z. Lei, Z.-J. Guan, X.-L. Pei, S.-F. Yuan, X.-K. Wan, J.-Y. Zhang and Q.-M. Wang, *Chem. Eur. J.*, 2016, **22**, 11156–11160.
226 L. He, J. Yuan, N. Xia, L. Liao, X. Liu, Z. Gan, C. Wang, J. Yang and Z. Wu, *J. Am. Chem. Soc.*, 2018, **140**, 3487–3490.
227 L. He, Z. Gan, N. Xia, L. Liao and Z. Wu, *Angew. Chem. Int. Ed.*, 2019, **58**, 9897–9901.
228 S.-S. Zhang, H.-F. Su, Z. Wang, X.-P. Wang, W.-X. Chen, Q.-Q. Zhao, C.-H. Tung, D. Sun and L.-S. Zheng, *Chem. Eur. J.*, 2018, **24**, 1998–2003.
229 J.-W. Liu, L. Feng, H.-F. Su, Z. Wang, Q.-Q. Zhao, X.-P. Wang, C.-H. Tung, D. Sun and L.-S. Zheng, *J. Am. Chem. Soc.*, 2018, **140**, 1600–1603.
230 Y.-M. Su, Z. Wang, G.-L. Zhuang, Q.-Q. Zhao, X.-P. Wang, C.-H. Tung and D. Sun, *Chem. Sci.*, 2019, **10**, 564–568.

231 J.-W. Liu, H.-F. Su, Z. Wang, Y.-A. Li, Q.-Q. Zhao, X.-P. Wang, C.-H. Tung, D. Sun and L.-S. Zheng, *Chem. Commun.*, 2018, **54**, 4461–4464.
232 X.-K. Wan, Q. Tang, S.-F. Yuan, D. -e. Jiang and Q.-M. Wang, *J. Am. Chem. Soc.*, 2015, **137**, 652–655.
233 Z. Lei, X.-K. Wan, S.-F. Yuan, Z.-J. Guan and Q.-M. Wang, *Acc. Chem. Res.*, 2018, **51**, 2465–2474.
234 X.-S. Han, X. Luan, H.-F. Su, J.-J. Li, S.-F. Yuan, Z. Lei, Y. Pei and Q.-M. Wang, *Angew. Chem. Int. Ed.*, 2020, **59**, 2309–2312.
235 S. Yang, J. Chai, Y. Lv, T. Chen, S. Wang, H. Yu and M. Zhu, *Chem. Commun.*, 2018, **54**, 12077–12080.
236 L. Huang, J. Yan, L. Ren, B. K. Teo and N. Zheng, *Dalton Trans.*, 2017, **46**, 1757–1760.
237 H. Yang, J. Yan, Y. Wang, G. Deng, H. Su, X. Zhao, C. Xu, B. K. Teo and N. Zheng, *J. Am. Chem. Soc.*, 2017, **139**, 16113–16116.
238 Y. Song, F. Fu, J. Zhang, J. Chai, X. Kang, P. Li, S. Li, H. Zhou and M. Zhu, *Angew. Chem. Int. Ed.*, 2015, **54**, 8430–8434.
239 Y. Song, Y. Li, H. Li, F. Ke, J. Xiang, C. Zhou, P. Li, M. Zhu and R. Jin, *Nat. Commun.*, 2020, 11:478.
240 H. Yang, Y. Wang, X. Chen, X. Zhao, L. Gu, H. Huang, J. Yan, C. Xu, G. Li, J. Wu, A. J. Edwards, B. Dittrich, Z. Tang, D. Wang, L. Lehtovaara, H. Häkkinen and N. Zheng, *Nat. Commun.*, 2016, 7:12809.
241 Y. Song, K. J. Lambright, M. Zhou, K. Kirschbaum, J. Xiang, A. Xia, M. Zhu and R. Jin, *ACS NANO*, 2018, **12**, 9318–9325.
242 T. Higaki, C. Liu, D. J. Morris, G. He, T.-Y. Luo, M. Y. Sfeir, P. Zhang, N. L. Rosi and R. Jin, *Angew. Chem. Int. Ed.*, 2019, **58**, 18798–18802.
243 X.-K. Wan, J.-Q. Wang and Q.-M. Wang, *Angew. Chem. Int. Ed.*, 2021, **60**, 20748–20753.
244 Y. Li, T.-Y. Luo, M. Zhou, Y. Song, N. L. Rosi and R. Jin, *J. Am. Chem. Soc.*, 2018, **140**, 14235–14243.
245 C. Xu, Y. Zhou, L. Shi and L. Cheng, *J. Phys. Chem. Lett.*, 2022, **13**, 10147–10152.
246 R.-W. Huang, J. Yin, C. Dong, A. Ghosh, M. J. Alhilaly, X. Dong, M. N. Hedhili, E. Abou-Hamad, B. Alamer, S. Nematulloev, Y. Han, O. F. Mohammed and O. M. Bakr, *J. Am. Chem. Soc.*, 2020, **142**, 8696–8705.
247 H. Soo Choi, W. Liu, P. Misra, E. Tanaka, J. P. Zimmer, B. Itty Ipe, M. G. Bawendi and J. V. Frangioni, *Nat. Biotechnol.*, 2007, **25**, 1165–1170.
248 B. Du, X. Jiang, A. Das, Q. Zhou, M. Yu, R. Jin and J. Zheng, *Nat. Nanotechnol.*, 2017, **12**, 1096–1102.
249 C. N. Loynachan, A. P. Soleimany, J. S. Dudani, Y. Lin, A. Najer, A. Bekdemir, Q. Chen, S. N. Bhatia and M. M. Stevens, *Nature Nanotechnology*, 2019, **14**, 883–890.
250 C. J. Murphy and N. R. Jana, *Adv. Mater.*, 2002, **14**, 80–82.
251 R. Takahata, S. Yamazoe, K. Koyasu, K. Imura and T. Tsukuda, *J. Am. Chem. Soc.*, 2018, **140**, 6640–6647.
252 Q. Yao, L. Liu, S. Malola, M. Ge, H. Xu, Z. Wu, T. Chen, Y. Cao, M. F. Matus, A. Pihlajamäki, Y. Han, H. Häkkinen and J. Xie, *Nature Chemistry*, , DOI:10.1038/s41557-022-01079-9.
253 H. Zhang, H. Liu, Z. Tian, D. Lu, Y. Yu, S. Cestellos-Blanco, K. K. Sakimoto and P. Yang, *Nature nanotechnology*, 2018, **13**, 900–905.
254 H. Liu, G. Hong, Z. Luo, J. Chen, J. Chang, M. Gong, H. He, J. Yang, X. Yuan, L. Li, X. Mu, J. Wang, W. Mi, J. Luo, J. Xie and X.-D. Zhang, *Adv. Mater.*, 2019, **31**, 1901015.
255 S. Kumar and R. Jin, *Nanoscale*, 2012, **4**, 4222–4227.
256 T. Chen, V. Fung, Q. Yao, Z. Luo, D. Jiang and J. Xie, *J. Am. Chem. Soc.*, 2018, **140**, 11370–11377.
257 L. H. Tan, H. Xing, H. Chen and Y. Lu, *J. Am. Chem. Soc.*, 2013, **135**, 17675–17678.
258 G. Chen, K. J. Gibson, D. Liu, H. C. Rees, J.-H. Lee, W. Xia, R. Lin, H. L. Xin, O. Gang and Y. Weizmann, *Nat. Mater.*, 2019, **18**, 169–174.
259 S. Sheikholeslami, Y. Jun, P. K. Jain and A. P. Alivisatos, *Nano Lett.*, 2010, **10**, 2655–2660.
260 J. Jiang, H. Gu, H. Shao, E. Devlin, G. C. Papaefthymiou and J. Y. Ying, *Adv. Mater.*, 2008, **20**, 4403–4407.
261 R. Jin, Y. W. Cao, C. A. Mirkin, K. L. Kelly, G. C. Schatz and J. G. Zheng, *Science*, 2001, **294**, 1901–1903.
262 S. S. Shankar, A. Rai, B. Ankamwar, A. Singh, A. Ahmad and M. Sastry, *Nat. Mater.*, 2004, **3**, 482–488.
263 L. J. Sherry, R. Jin, C. A. Mirkin, G. C. Schatz and R. P. Van Duyne, *Nano Lett.*, 2006, **6**, 2060–2065.
264 T. H. Ha, H.-J. Koo and B. H. Chung, *J. Phys. Chem. C*, 2007, **111**, 1123–1130.
265 J. E. Millstone, G. S. Métraux and C. A. Mirkin, *Adv. Funct. Mater.*, 2006, **16**, 1209–1214.
266 H. Häkkinen, *Nat. Chem.*, 2012, **4**, 443–455.